

Accepted Manuscript

An Accurate and Computationally Efficient Uniaxial Phenomenological Model for Steel and Fiber Reinforced Elastomeric Bearings

Nicolò Vaiana, Salvatore Sessa, Francesco Marmo, Luciano Rosati

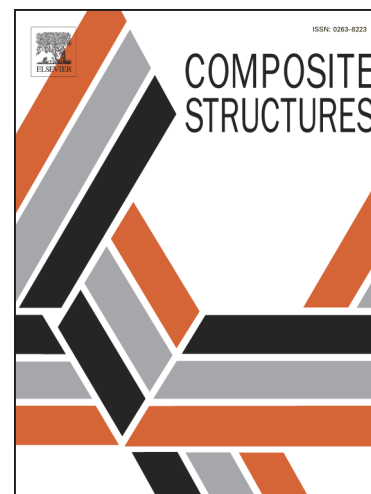
PII: S0263-8223(18)32935-0
DOI: <https://doi.org/10.1016/j.compstruct.2018.12.017>
Reference: COST 10480

To appear in: *Composite Structures*

Received Date: 10 August 2018
Revised Date: 27 November 2018
Accepted Date: 11 December 2018

Please cite this article as: Vaiana, N., Sessa, S., Marmo, F., Rosati, L., An Accurate and Computationally Efficient Uniaxial Phenomenological Model for Steel and Fiber Reinforced Elastomeric Bearings, *Composite Structures* (2018), doi: <https://doi.org/10.1016/j.compstruct.2018.12.017>

This is a PDF file of an unedited manuscript that has been accepted for publication. As a service to our customers we are providing this early version of the manuscript. The manuscript will undergo copyediting, typesetting, and review of the resulting proof before it is published in its final form. Please note that during the production process errors may be discovered which could affect the content, and all legal disclaimers that apply to the journal pertain.



An Accurate and Computationally Efficient Uniaxial Phenomenological Model for Steel and Fiber Reinforced Elastomeric Bearings

Nicolò Vaiana^{a,*}, Salvatore Sessa^a, Francesco Marmo^a, Luciano Rosati^a

^aDepartment of Structures for Engineering and Architecture, University of Naples Federico II, Via Claudio, 21, 80124, Napoli, Italy

Abstract

We present a uniaxial phenomenological model to accurately predict the complex hysteretic behavior of bolted steel reinforced elastomeric bearings and unbonded fiber reinforced elastomeric bearings. The proposed model is based on a set of only five parameters, directly associated with the graphical properties of the hysteresis loop, leads to the solution of an algebraic equation for the evaluation of the isolator restoring force, requires only one history variable, and can be easily implemented in a computer program. The proposed model is validated by means of experimental tests and numerical simulations. In particular, the results predicted analytically are compared with some experimental results selected from the literature. Furthermore, numerical accuracy and computational efficiency of the model are assessed by performing nonlinear time history analyses on a single degree of freedom mechanical system and comparing the results with those associated with a modified version of the celebrated Bouc-Wen model.

Keywords: Elastomeric bearing, Steel reinforcement, Fiber reinforcement, Phenomenological model, Accuracy, Computational efficiency

1. Introduction

Elastomeric bearings are seismic isolation devices made up of alternating layers of rubber and thin reinforcing elements [1, 2]. Looking at the type of reinforcement, it is possible to distinguish between Steel Reinforced Elastomeric Bearings (SREBs) and Fiber Reinforced Elastomeric Bearings (FREBs). The former are generally adopted in traditional bolted applications [2], whereas the latter are typically used in unbonded applications [3].

The hysteretic behavior displayed by bolted SREBs and unbonded FREBs is significantly different [4–7].

A large number of uniaxial phenomenological models have been proposed in the literature for simulating the complex hysteretic behavior occurring in elastomeric bearings when they deform along their transverse directions under the effect of a constant axial compressive load.

Depending on the kind of equation that needs to be solved for the evaluation of the output variable (e.g., restoring force), such models can be classified into three main categories: i) algebraic models, ii) transcendental models, and iii) differential models.

Among existing algebraic models, the bilinear model is the simplest and most used one for the simulation of hysteresis phenomena occurring in elastomeric bearings [1, 8]. The model, based on a set of only three parameters having a clear mechanical significance, can be employed when the device reaches relatively large shear strains, that is, shear strains smaller than 100-150%; indeed, such a model is not able to simulate the more complex behavior typically displayed by elastomeric bearings

at greater shear strains. Furthermore, in order to accurately predict the actual behavior of elastomeric devices, the parameters of the bilinear model need to be updated, by means of an iterative procedure, according to the transverse displacement value reached at each reversal point of the hysteretic response [9, 10].

Markou and Manolis [11] extended the bilinear model by developing two trilinear models, based on thirty and thirty-three parameters, respectively, to reproduce the complex behavior displayed by elastomeric bearings at large shear strains, that is, shear strains greater than 100-150%.

As regards transcendental models, Kikuchi and Aiken [12] and Hwang et al. [13] proposed two different models able to predict the response of bolted SREBs displaying highly nonlinear stiffening behavior at large shear strains due to a strain crystallization process in the rubber [14]. These two models adopt a set of twenty-three and ten parameters, respectively, having no clear mechanical significance. The Hwang et al. model [13] has been adopted by Toopchi-Nezhad et al. [10] for the simulation of the hysteretic response of unbonded FREBs, in conjunction with an iterative procedure used to update the model parameters during the performed nonlinear time history analyses.

As far as differential models are concerned, Nagarajaiah et al. [15] adopted the Bouc-Wen model [16–18], that is one of the widely used differential models in the literature, to predict the response of bolted SREBs at relatively large shear strains; this model, based on a set of seven parameters having no clear mechanical significance, is not able to simulate the stiffening behavior displayed by SREBs at shear strains greater than 100-150%. Chen and Ahmadi [19] and Tsai et al. [20] proposed two improved versions of the Bouc-Wen model [16–18], both based on a set of ten parameters, to take into account the highly non-

*Corresponding author

Email address: nicolovaiana@outlook.it (Nicolò Vaiana)

linear stiffening behavior displayed by bolted SREBs at large shear strains, whereas Manzoori and Toopchi-Nezhad [21] proposed a modified Bouc-Wen model [16–18], based on a set of ten parameters, to accurately reproduce the complex hysteretic behavior of unbonded FREBs.

The above-described existing uniaxial phenomenological models have different characteristics in terms of accuracy, computational efficiency, as well as number and mechanical significance of the adopted parameters. Among the existing models, differential models seem to be the most suitable ones to perform nonlinear dynamic analyses of actual base-isolated structures since they allow for an accurate prediction of the hysteretic response of elastomeric bearings by using a relatively small number of parameters whose values remain constant throughout the analysis. Unfortunately, such models are not computationally efficient because they require the numerical solution of a differential equation, generally solved by employing multi-steps [22] or Runge-Kutta methods [23], for each time step of a nonlinear time history analysis; in addition, such models adopt parameters having no clear mechanical significance, thus making difficult their calibration and use in practical applications.

This paper presents a uniaxial phenomenological model able to predict the hysteretic behavior typically displayed by bolted SREBs and unbonded FREBs, deforming along one of their transverse directions under the effect of a constant moderate axial compressive load, namely, an axial load that is significantly lower than the buckling load of the bearing. The proposed model, representing a specific instance of the class of uniaxial phenomenological models formulated by Vaiana et al. [24] for simulating hysteretic phenomena in rate-independent mechanical systems and materials, is an algebraic model since the output variable, having the mechanical meaning of device restoring force, is evaluated by solving an algebraic equation.

Compared to existing uniaxial phenomenological models developed for elastomeric bearings, the proposed one not only offers the important advantage of accurately simulating the response of such devices, but also allows for a considerable reduction of the computational effort required by nonlinear time history analyses. Indeed, the proposed model needs neither the numerical solution of a differential equation at each time step of the analysis for the evaluation of the output variable (i.e., restoring force), nor the use of an iterative procedure to update the model parameters during the analysis. Furthermore, the proposed algebraic model is based on a set of only five parameters having a clear mechanical significance and it can be easily implemented in a computer program.

The present paper is organized into three parts. For the reader's convenience, the main characteristics of SREBs and FREBs are illustrated in the first part (Section 2), with particular emphasis on the description of the hysteretic behavior displayed along their transverse directions under the effect of moderate axial compressive loads.

In the second part, the class of hysteretic models formulated by Vaiana et al. [24] is first summarized (Section 3) and the proposed uniaxial phenomenological model is developed (Section 4); subsequently, the parameter sensitivity analysis is carried out and a schematic flowchart of the proposed model is illus-

trated to allow for an easy computer implementation.

Finally, in the third part (Section 5), the proposed model is validated by means of experimental tests, retrieved in the literature, as well as numerical simulations.

2. Elastomeric Bearings

Elastomeric bearings are seismic isolation devices made up of alternating sheets of rubber and thin reinforcing elements. The rubber layers provide flexibility and energy dissipation capacity along the device transverse directions, whereas the reinforcing elements not only prevent the transverse bulging of the elastomer when the device is subjected to axial compressive loads, but also provide a large axial stiffness, generally several hundred times greater than the transverse one [2].

According to the type of adopted reinforcing elements, elastomeric bearings can be classified into two main categories, namely, *Steel Reinforced Elastomeric Bearings* and *Fiber Reinforced Elastomeric Bearings*. The former adopt thin steel plates as reinforcement [25], whereas the latter employ thin layers of fiber fabric [26].

In this section, the main characteristics of the two above-mentioned types of elastomeric bearings are illustrated with particular emphasis on the description of the hysteretic behavior displayed along their transverse directions under the effect of moderate axial compressive loads.

2.1. Steel Reinforced Elastomeric Bearings

Steel Reinforced Elastomeric Bearings (SREBs) are currently the most widely used seismic isolation devices adopted for the seismic protection of structures and equipment in buildings, although their application is limited due to the high manufacturing and installation costs [1].

Typically, conventional SREBs have a symmetrically shaped transverse cross section, that is, circular or square, and are made of alternating layers of rubber and thin steel reinforcing plates which are bonded together by means of a vulcanization process. Furthermore, such bearings have two thick steel plates bounded to the top and bottom surfaces, respectively, that allow for their connection to the structure [25].

Three main types of SREBs have been proposed and implemented in actual base isolation systems, namely, Low Damping Rubber Bearings (LDRBs), High Damping Rubber Bearings (HDRBs), and Lead Rubber Bearings (LRBs). LDRBs are elastomeric bearings made of natural or synthetic rubber and characterized by low energy dissipation properties.

On the contrary, HDRBs and LRBs are elastomeric bearings able to dissipate large amounts of energy. Specifically, in HDRBs, the increase in the amount of dissipated energy is reached by adding extra fine carbons, oils, resins, or other proprietary fillers to the natural rubber compound, whereas, in LRBs, it is reached by inserting a cylinder of lead into a hole in the core of the bearing [1].

SREBs can be employed in two different types of application, namely, bolted and dowelled applications. In bolted bearings deforming along one of their transverse directions, significant

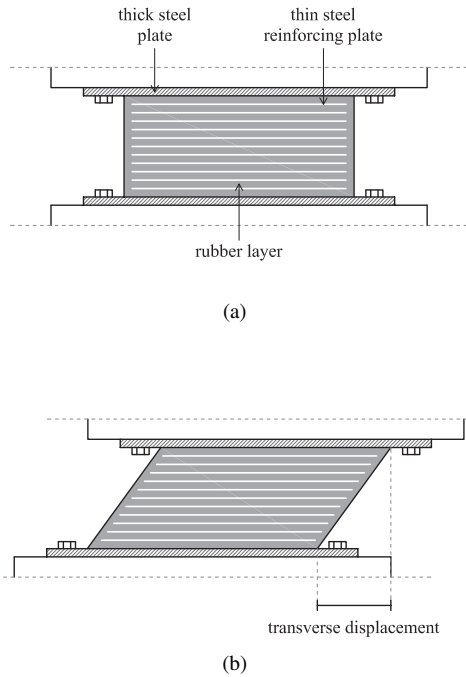


Figure 1: Sectional views of a typical bolted SREB in undeformed (a) and deformed (b) configuration

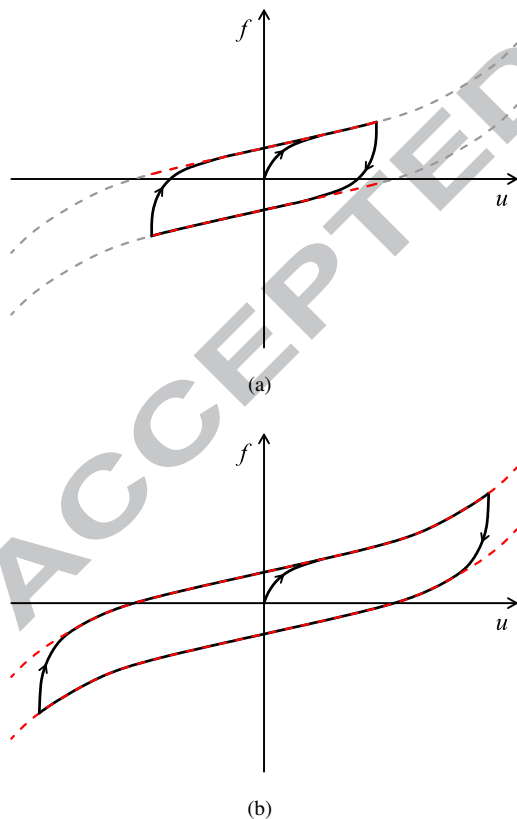


Figure 2: Typical hysteresis loop displayed by bolted SREBs at (a) relatively large ($\gamma \leq 100-150\%$) and (b) large ($\gamma > 100-150\%$) shear strains

tensile stresses occur in the regions outside the central compress-

ion core, that is, the overlap region between top and bottom surfaces. On the contrary, in dowelled bearings, the occurring tensile stresses are negligible [2].

In practice, such devices are generally adopted in bolted applications [2], so that only the hysteretic behavior displayed by bolted SREBs is of specific interest in this paper.

Figure 1 shows the sectional views of a typical bolted SREB in undeformed (Figure 1a) and deformed (Figure 1b) configurations.

The hysteretic behavior displayed by a bolted SREB deforming along one of its transverse directions under the effect a constant moderate axial compressive load, namely, an axial load that is significantly lower than the buckling load of the bearing, is generally characterized by kinematic hardening since the device restoring force f increases with the device transverse displacement u . Note that the increasing values of the device restoring force f as a function of increasing values of the device transverse displacement u , what typically characterizes hardening, have not to be confused with the behavior of the tangent stiffness df/du whose value is positive (negative) when hardening (softening) occurs. Specifically, the hysteresis loop shape depends on the value of the shear strain attained by the bearing, γ , typically defined as the ratio of the device transverse displacement to the total thickness of the rubber layers [25, 27].

According to experimental test results available in the literature, it can be observed that, for relatively large shear strains (e.g., $\gamma \leq 100-150\%$), the typical hysteresis loop is limited by two parallel straight lines, as shown in Figure 2a, whereas, for large shear strains (e.g., $\gamma > 100-150\%$), the two bounds of the typical hysteresis loop become two parallel curves, as shown in Figure 2b. In this last case, an increase of the tangent stiffness, df/du , occurs due to strain crystallization of the rubber matrix [14, 28].

It has to be noted that the exact shear strain value corresponding to the beginning of the tangent stiffness increase depends on the type of the rubber adopted in the bearing; generally speaking, in HDRBs, such a tangent stiffness increase occurs at smaller shear strains than that of LDRBs and LRBs. It has also to be pointed out that, although the hysteresis loops of the three types of bolted SREBs are similar in shape, HDRBs (LDRBs) display loops having the largest (smallest) value of enclosed area associated with the same assigned value of device transverse displacement [29].

2.2. Fiber Reinforced Elastomeric Bearings

Fiber Reinforced Elastomeric Bearings (FREBs) represent a new category of elastomeric bearings, currently object of many research studies aimed at their experimental characterization as well as mathematical modeling. Compared to conventional SREBs, FREBs offer several important advantages, such as low manufacturing and installation costs and superior energy dissipation capability [30, 31].

Typically, FREBs have a circular, square, or rectangular transverse cross section and are made of alternating layers of rubber and fiber reinforcement which are bonded together by means of a vulcanization process [32]. Fiber reinforcing fabrics, consisting of cords made from individual fibers grouped

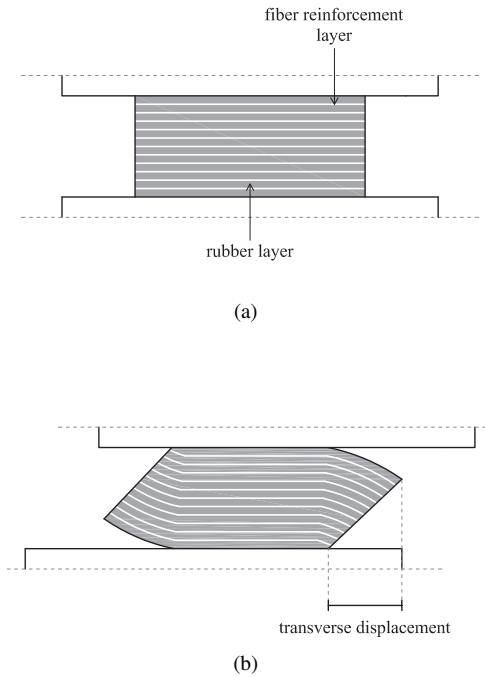


Figure 3: Sectional views of a typical unbonded FREB in undeformed (a) and deformed (b) configuration

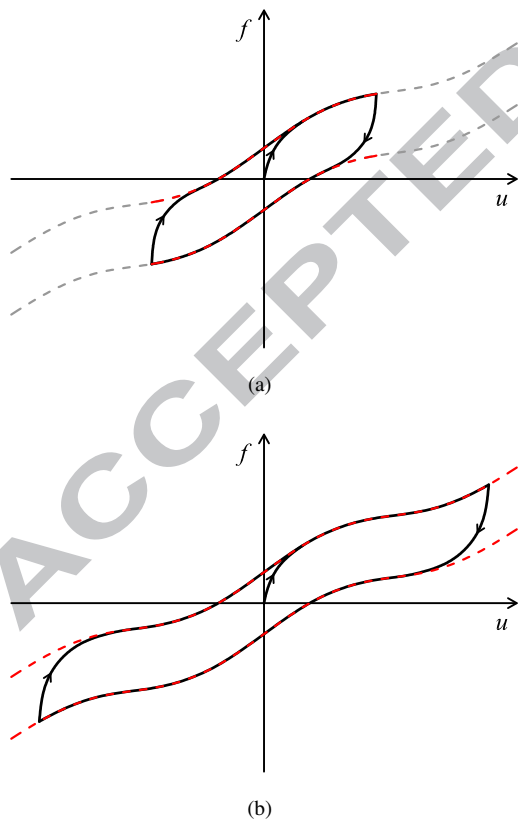


Figure 4: Typical hysteresis loop displayed by stable unbonded FREBs at (a) relatively large ($\gamma \leq 100-150\%$) and (b) large ($\gamma > 100-150\%$) shear strains

and coiled together [4], are generally manufactured by adopt-

ing a bi-directional or quadri-directional layout [8] and by using one of the different kinds of available fibers, such as carbon, glass, nylon, and polyester fibers [33].

FREBs can be employed in two different types of application, namely, bonded and unbonded applications. Bonded FREBs are connected to the structure by means of two thick steel plates bonded, respectively, to the top and bottom surfaces of the device, whereas unbonded FREBs are simply placed between the substructure and superstructure without any type of mechanical or chemical bonding. In bonded devices deforming along one of their transverse directions, significant tensile stresses occur in the regions outside the central compression core, that is, the overlap region between top and bottom surfaces. On the contrary, in unbonded bearings, the occurring tensile stresses are negligible [5].

Such devices are generally adopted in unbonded applications [3], being unbonded FREBs considerably more efficient than bonded FREBs [31]; thus, only the hysteretic behavior displayed by unbonded FREBs is of specific interest in this paper.

Figure 3 shows the sectional views of a typical unbonded FREB in undeformed (Figure 3a) and deformed (Figure 3b) configurations. As illustrated in Figure 3b, when the bearing deforms along one of its transverse directions, some regions of its top and bottom surface detach from the structure; in the literature, this phenomenon, occurring due to the unbonded application as well as the lack of flexural rigidity of the adopted reinforcement elements, is referred to as *rollover*. At a certain value of the transverse displacement, when the originally vertical surfaces of the bearing completely contact the horizontal surfaces of the structure, the so-called *full rollover* occurs [34].

The hysteretic behavior displayed by a stable unbonded FREB deforming along one of its transverse directions under the effect of a constant moderate axial compressive load, namely, an axial load that is significantly lower than the buckling load of the bearing, is generally characterized by kinematic hardening since the device restoring force f increases with the device transverse displacement u [34]. Specifically, the hysteresis loop shape depends on the value of the shear strain reached by the bearing, γ , typically defined as the ratio of the device transverse displacement to the total thickness of the rubber layers [26, 35].

According to experimental test results available in the literature, it can be observed that, for relatively large shear strains (e.g., $\gamma \leq 100-150\%$), the typical hysteresis loop is limited by two parallel curves characterized by one inflection point, as shown in Figure 4a. For large shear strains (e.g., $\gamma > 100-150\%$), the two bounds of the typical hysteresis loop become two parallel curves having three inflection points, as shown in Figure 4b. The increase of the transverse tangent stiffness, df/du , with the transverse displacement, u , is due to the full rollover [31, 36].

It has to be noted that, in FREBs having square or rectangular transverse cross section, the exact shear strain value corresponding to the beginning of the transverse tangent stiffness increase depends on the loading direction; as an example, in a square unbonded FREB deforming along a transverse direction parallel to one of its sides, such a tangent stiffness increase

occurs at smaller shear strains than that of the same device deforming along one of its diagonal directions [31, 35].

3. Review of a Class of Phenomenological Models

The hysteretic behavior displayed by the elastomeric bearings, described in Section 2, is generally modeled in the literature [11–13, 19, 21, 37–40] by adopting two springs in parallel, that is, a uniaxial hysteretic spring and a nonlinear elastic one. The former, having tangent stiffness k_h , is able to simulate hysteresis loops limited by two straight lines, whereas the latter, having tangent stiffness k_e , is able to modify the shape of the straight lines, thus obtaining two limiting curves.

Such a basic idea has been generalized by Vaiana et al. [24], who have recently proposed a general formulation of a class of uniaxial phenomenological models able to accurately simulate rate-independent mechanical hysteretic phenomena having a generalized displacement u , that is, displacement, rotation or strain, as input, and a generalized force f , that is, force, moment or stress, as output.

In the following section, the above-mentioned class of hysteretic models is summarized in order to introduce the proposed model, developed in Section 4. Specifically, as done in the original work by Vaiana et al. [24], the adopted nomenclature is first described; then, the general expression of the generalized tangent stiffness k_t , obtained as the sum of k_h and k_e , as well as the general expressions of the generalized force and history variable are presented.

3.1. Preliminaries

In the general formulation proposed by Vaiana et al. [24], a typical generalized force-displacement hysteresis loop is characterized by four types of curves, namely, the upper and the lower limiting curves, denoted as c_u and c_l , respectively, and the generic loading and unloading curves, denoted as c^+ and c^- , respectively.

Figure 5a (5b) shows the curves c_u , c_l , c^+ , and c^- for a hysteresis loop bounded by two parallel straight lines (curves). Two arrows have been plotted to identify the generic loading and unloading curves, characterized, respectively, by a positive and negative sign of the generalized velocity \dot{u} , namely, the first time derivative of the generalized displacement u .

As shown in Figure 5, the upper limiting curve c_u intercepts the vertical axis at $f = \bar{f}$, whereas the lower limiting curve c_l intercepts the vertical axis at $f = -\bar{f}$. The distance between the two curves, along the vertical axis, is assumed to be constant and equal to $2\bar{f}$ since the formulation by Vaiana et al. [24] assumes that the limiting curves are not affected by cyclic loading phenomena.

The generic loading curve c^+ has a starting (ending) point, lying on the lower (upper) limiting curve c_l (c_u), having abscissa u_i^+ (u_j^+), with $u_i^+ = u_j^+ - 2u_0$. Similarly, the generic unloading curve c^- has a starting (ending) point, lying on the upper (lower) limiting curve c_u (c_l), having abscissa u_i^- (u_j^-), with $u_i^- = u_j^- + 2u_0$.

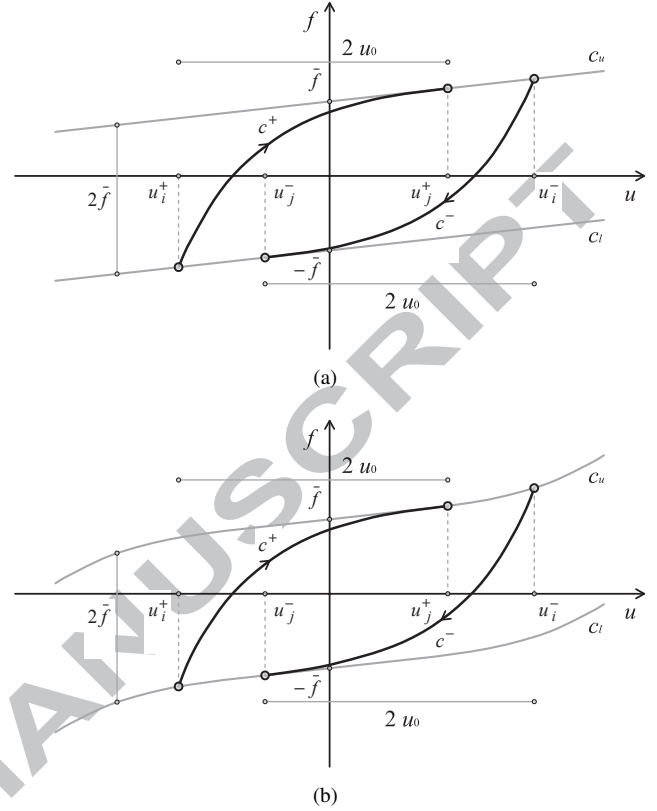


Figure 5: Curves c_u , c_l , c^+ , and c^- for a hysteresis loop bounded by two parallel straight lines (a) or curves (b)

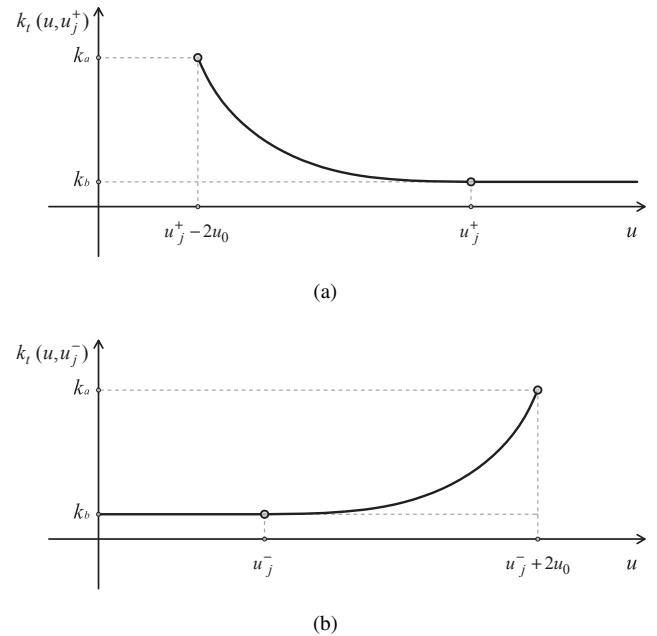


Figure 6: Graph of the generalized tangent stiffness k_t for a generic loading (a) and unloading (b) case in Figure 5a

The superscript + (–) denotes generic loading (unloading) curves, whereas the subscript i (j) is reminiscent of the starting (ending) points of each curve.

3.2. Generalized Tangent Stiffness

In the formulation by Vaiana et al. [24], the general expression of the generalized tangent stiffness k_t , specialized for the generic loading ($\dot{u} > 0$) and unloading ($\dot{u} < 0$) cases, is:

$$k_t(u, u_j^+) = k_e(u) + k_h(u, u_j^+) \quad \text{when } \dot{u} > 0, \quad (1a)$$

$$k_t(u, u_j^-) = k_e(u) + k_h(u, u_j^-) \quad \text{when } \dot{u} < 0, \quad (1b)$$

where $k_e(u)$ is a function of the absolute generalized displacement u , whereas $k_h(u, u_j^+)$ ($k_h(u, u_j^-)$) is a function of a relative generalized displacement evaluated by relating u to the history variable u_j^+ (u_j^-).

As an example, the graph of function $k_t(u, u_j^+)$ ($k_t(u, u_j^-)$), characterizing the generic loading (unloading) curve c^+ (c^-) of Figure 5a, is illustrated in Figure 6a (6b). In particular, being $k_e(u) = 0$, the generalized tangent stiffness function nonlinearly decreases, from k_a to k_b , on $[u_j^+ - 2u_0, u_j^+]$, when $\dot{u} > 0$, and on $[u_j^-, u_j^- + 2u_0]$, when $\dot{u} < 0$; moreover, it is constant and equal to k_b on $[u_j^+, \infty)$, when $\dot{u} > 0$, and on $(-\infty, u_j^-]$, when $\dot{u} < 0$.

3.3. Generalized Force

According to Figure 5, the general expression of the generalized force f , for a generic loading case ($\dot{u} > 0$), is:

$$f(u, u_j^+) = \begin{cases} c^+(u, u_j^+) & u \in [u_j^+ - 2u_0, u_j^+] \\ c_u(u) & u \in [u_j^+, \infty) \end{cases} \quad (2a)$$

$$(2b)$$

whereas, for a generic unloading case ($\dot{u} < 0$), it becomes:

$$f(u, u_j^-) = \begin{cases} c^-(u, u_j^-) & u \in [u_j^-, u_j^- + 2u_0] \\ c_l(u) & u \in (-\infty, u_j^-] \end{cases} \quad (3a)$$

$$(3b)$$

The integration of the generalized tangent stiffness k_t , given by Equation (1), allows one to derive the general expressions for the upper and lower limiting curves, and for the generic loading and unloading curves.

Specifically, the general expression of the upper limiting curve, obtained by integrating Equation (1a) with $u \geq u_j^+$, so that $k_h(u, u_j^+)$ is constant and equal to k_b , and by imposing that the curve c_u intercepts the vertical axis at $f = \bar{f}$, to determine the integration constant, is:

$$\text{eq: 4} \quad c_u(u) = f_e(u) + k_b u + \bar{f}, \quad (4)$$

whereas, the general expression of the lower limiting curve, obtained by integrating Equation (1b) with $u \leq u_j^-$, so that $k_h(u, u_j^-)$ is constant and equal to k_b , and by imposing that the curve c_l intercepts the vertical axis at $f = -\bar{f}$, to evaluate the integration constant, is:

$$\text{eq: 5} \quad c_l(u) = f_e(u) + k_b u - \bar{f}, \quad (5)$$

where:

$$\text{eq: 6} \quad f_e(u) = \int k_e(u) du. \quad (6)$$

Furthermore, the general expression of the generic loading curve, obtained by integrating Equation (1a) with $u_i^+ \leq u \leq u_j^+$, and by imposing that the generic loading curve c^+ intersects the upper limiting curve c_u at $u = u_j^+$, to determine the integration constant, is:

$$c^+(u, u_j^+) = f_e(u) + f_h(u, u_j^+) + k_b u_j^+ + \bar{f} - f_h(u_j^+, u_j^+), \quad (7) \quad \{\text{eq: e}\}$$

whereas, the general expression of the generic unloading curve, obtained by integrating Equation (1b) with $u_j^- \leq u \leq u_i^-$, and by imposing that the generic unloading curve c^- intersects the lower limiting curve c_l at $u = u_j^-$, to evaluate the integration constant, is:

$$c^-(u, u_j^-) = f_e(u) + f_h(u, u_j^-) + k_b u_j^- - \bar{f} - f_h(u_j^-, u_j^-), \quad (8) \quad \{\text{eq: e}\}$$

where:

$$f_h(u, u_j^+) = \int k_h(u, u_j^+) du, \quad (9) \quad \{\text{eq: e}\}$$

and

$$f_h(u, u_j^-) = \int k_h(u, u_j^-) du. \quad (10) \quad \{\text{eq: e}\}$$

The model parameters \bar{f} and u_0 are related by a general expression that can be solved for \bar{f} or u_0 , either in closed form or numerically, depending on the complexity of function f_h derived from the integration of the selected generalized tangent stiffness function k_h . Such an expression, obtained by imposing that the generic loading curve c^+ intersects the lower limiting curve at $u = u_i^+$, and by remembering that $u_i^+ = u_j^+ - 2u_0$, is:

$$f_h(u_j^+ - 2u_0, u_j^+) + 2k_b u_0 + 2\bar{f} - f_h(u_j^+, u_j^+) = 0. \quad (11) \quad \{\text{eq: e}\}$$

An analogous general expression that complements Equation (11), obtained by imposing that the generic unloading curve c^- intersects the upper limiting curve at $u = u_i^-$, and by remembering that $u_i^- = u_j^- + 2u_0$, is:

$$f_h(u_j^- + 2u_0, u_j^-) - 2k_b u_0 - 2\bar{f} - f_h(u_j^-, u_j^-) = 0. \quad (12) \quad \{\text{eq: e}\}$$

3.4. History Variable

The expression of u_j^+ (u_j^-), that is, the generalized displacement required to evaluate the generalized force f in the generic loading (unloading) case, needs to be derived for a generic starting point P , namely, a point that does not lie on the lower (upper) limiting curve, for which u_j^+ (u_j^-) cannot be computed as $u_j^+ = u_i^+ + 2u_0$ ($u_j^- = u_i^- - 2u_0$). Indeed, as shown in Figure 7, when a generic loading (unloading) curve has an initial point $P : (u_P, f_P)$ that lies between the two limiting curves, the distance, along the horizontal axis, between the starting and ending points of the curve is equal to $u_j^+ - u_P$ ($|u_j^- - u_P|$) and, thus, it becomes smaller than $2u_0$.

The general expression for the evaluation of the history variable u_j^+ , obtained by imposing that the generic loading curve c^+

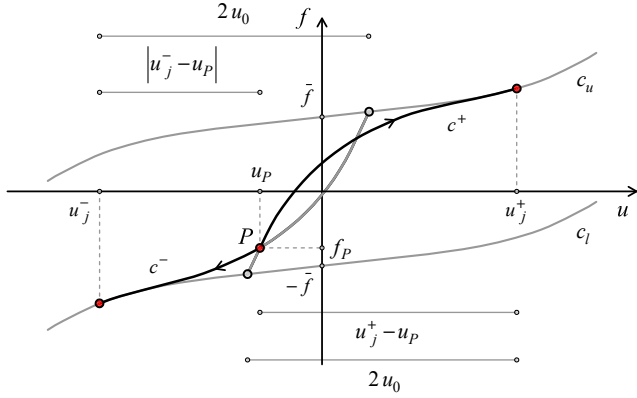


Figure 7: Evaluation of the history variable u_j^+ (u_j^-) for a generic loading (unloading) case

passes through the point $P : (u_P, f_P)$, as shown in Figure 7, is:

$$f_e(u_P) + f_h(u_P, u_j^+) + k_b u_j^+ + \bar{f} - f_h(u_j^+, u_j^+) = f_P, \quad (13)$$

whereas, the general expression for the evaluation of the history variable u_j^- , obtained by imposing that the generic unloading curve c^- passes through the point $P : (u_P, f_P)$, as shown in Figure 7, is:

$$f_e(u_P) + f_h(u_P, u_j^-) + k_b u_j^- - \bar{f} - f_h(u_j^-, u_j^-) = f_P. \quad (14)$$

Equations (13) and (14) can be solved for u_j^+ and u_j^- , respectively, in closed form or numerically, depending on the complexity of function f_h derived from the integration of the selected generalized tangent stiffness function k_h .

4. Proposed Hysteretic Model

In this section, using the general formulation summarized in Section 3, we first develop the proposed uniaxial phenomenological model, representing a specific instance of the general class formulated in Vaiana et al. [24], and show that it is able to simulate hysteresis loops limited by two parallel straight lines or curves by adopting a set of only five parameters. Subsequently, we examine the different hysteresis loop shapes, that can be reproduced by means of the proposed model, as well as the sensitivity of each model parameter in affecting the hysteresis loop size and/or shape. Finally, we present a schematic flowchart of the model to allow for an easy computer implementation.

For simplicity, in the sequel, the proposed model is denominated Algebraic Model (AM) since the generalized force, representing the output variable of the model, is evaluated by solving an algebraic equation.

Moreover, according to the nomenclature typically adopted in the literature to describe the behavior of seismic isolators deforming along one of their transverse directions, the generalized force, the generalized displacement, and the generalized tangent stiffness, introduced in Section 3 with respect to a generic mechanical system or material, are referred to as, respectively,

the restoring force, the transverse displacement, and the transverse tangent stiffness of an isolation device.

4.1. Algebraic Model

The development of the model, described in this subsection, consists in the selection of the transverse tangent stiffness functions, that is, k_e and k_h , and in the analytical derivation of the expressions for the restoring force and for the history variable.

4.1.1. Transverse tangent stiffness

The selection of the transverse tangent stiffness functions plays a crucial role in the model development since it directly affects the main model features, such as the accuracy, the computational efficiency, as well as the number and the mechanical significance of the model parameters.

The transverse tangent stiffness functions, proposed in this work, are:

$$k_e(u) = 13\beta_1 u^2 + 5\beta_2 u^4 \quad \text{on } (-\infty, \infty), \quad (15) \quad \{\text{eq: e}$$

$$k_h(u, u_j^+) = \begin{cases} k_b + \frac{k_a - k_b}{[1 + \bar{u}^{-1}(u - u_j^+ + 2u_0)]^\alpha} & \text{on } [u_j^+ - 2u_0, u_j^+] \\ k_b & \text{on }]u_j^+, \infty), \end{cases} \quad (16a) \quad (16b)$$

$$k_h(u, u_j^-) = \begin{cases} k_b + \frac{k_a - k_b}{[1 + \bar{u}^{-1}(-u + u_j^- + 2u_0)]^\alpha} & \text{on }]u_j^-, u_j^- + 2u_0] \\ k_b & \text{on } (-\infty, u_j^-], \end{cases} \quad (17a) \quad (17b)$$

where k_a , k_b , α , β_1 , and β_2 are model parameters to be identified from experimental tests, \bar{u} is a model parameter, assumed equal to one, formally introduced to non-dimensionalize the denominator in Equations (16a) and (17a), whereas u_0 is a model parameter that can be expressed as a function of k_a , k_b , and α , as demonstrated in the sequel. Specifically, $k_a > k_b$, $k_a > 0$, $\alpha > 0$, $\alpha \neq 1$, $u_0 > 0$, whereas β_1 and β_2 are reals.

The shape of function k_e depends on the parameters β_1 and β_2 ; in particular, if $\beta_1/\beta_2 > 0$, k_e has no inflection points and it is convex (concave) on $(-\infty, \infty)$, when β_1 and β_2 are positive (negative); on the contrary, if $\beta_1/\beta_2 < 0$, k_e has two inflection points and it is convex (concave) on the intervals $(-\infty, -\sqrt{-\beta_1/(10\beta_2)}]$ and $[\sqrt{-\beta_1/(10\beta_2)}, \infty)$, and concave (convex) on $[-\sqrt{-\beta_1/(10\beta_2)}, \sqrt{-\beta_1/(10\beta_2)}]$, when $\beta_1 < \beta_2$ ($\beta_1 > \beta_2$).

Function k_h is a nonlinearly decreasing function, from k_a to $k_b + (k_a - k_b)(1 + 2u_0)^{-\alpha}$, on $[u_j^+ - 2u_0, u_j^+]$, when $\dot{u} > 0$, and on $]u_j^-, u_j^- + 2u_0]$, when $\dot{u} < 0$; moreover, k_h is constant and equal to k_b on $]u_j^+, \infty)$, when $\dot{u} > 0$, and on $(-\infty, u_j^-]$, when $\dot{u} < 0$. The parameter α defines the velocity of variation of k_h , from k_a to $k_b + (k_a - k_b)(1 + 2u_0)^{-\alpha}$, as shown in Figure 8 for the generic loading case ($\dot{u} > 0$). The graph of function k_h for the generic unloading case ($\dot{u} < 0$) is omitted for brevity.

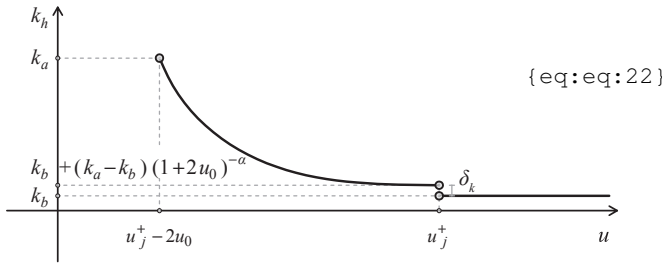


Figure 8: Graph of function k_h for the generic loading case

The internal model parameter u_0 can be expressed in terms of the parameters k_a , k_b , and α . Indeed, taking into account that k_h is discontinuous at u_j^+ (u_j^-), as shown in Figure 8 for the generic loading case, and denoting by δ_k the difference between the two different values assumed by the transverse tangent stiffness at u_j^+ (u_j^-), we can write:

$$\frac{k_a - k_b}{(1 + 2u_0)^\alpha} = \delta_k, \quad (18)$$

from which we obtain:

$$u_0 = \frac{1}{2} \left[\left(\frac{k_a - k_b}{\delta_k} \right)^{\frac{1}{\alpha}} - 1 \right], \quad (19)$$

an expression that yields positive values of u_0 for $0 < \delta_k < k_a - k_b$. In order to have a generic loading (unloading) curve c^+ (c^-) and an upper (lower) limiting curve c_u (c_l) with the same value of the transverse tangent stiffness at u_j^+ (u_j^-), we should set δ_k equal to zero in Equation (19), thus making u_0 undefined. However, the results of extensive numerical tests, only partially presented in this paper, suggest $\delta_k = 10^{-20}$ as a suitable value for practical purposes.

4.1.2. Restoring force

In the generic loading case, according to the general formulation described in Section 3, it turns out to be $f = c^+$ when $u_j^+ \leq u < u_j^+$, and $f = c_u$ when $u > u_j^+$, whereas, in the generic unloading case, $f = c^-$ when $u_j^- < u \leq u_j^-$, and $f = c_l$ when $u < u_j^-$. Thus, in the sequel, after deriving the expressions for the upper (lower) limiting curve c_u (c_l) and for the generic loading (unloading) curve c^+ (c^-), we obtain the expression of the internal model parameter \bar{f} required for the evaluation of c_u , c_l , c^+ , and c^- .

Upper and Lower Limiting Curves

According to the definition (6) and to the assumption (15), it turns out to be:

$$f_e(u) = \beta_1 u^3 + \beta_2 u^5. \quad (20)$$

Hence, Equation (4) yields:

$$c_u(u) = \beta_1 u^3 + \beta_2 u^5 + k_b u + \bar{f}, \quad (21)$$

whereas Equation (5) becomes:

$$c_l(u) = \beta_1 u^3 + \beta_2 u^5 + k_b u - \bar{f}. \quad (22)$$

Generic Loading and Unloading Curves

On account of the assumption (16a), Equation (9) specializes to:

$$f_h(u, u_j^+) = k_b u + (k_a - k_b) \frac{(1 + u - u_j^+ + 2u_0)^{(1-\alpha)}}{1 - \alpha}, \quad (23) \quad \{\text{eq: e}\}$$

so that, recalling (20), Equation (7) yields:

$$\begin{aligned} c^+(u, u_j^+) &= \beta_1 u^3 + \beta_2 u^5 + k_b u \\ &+ (k_a - k_b) \left[\frac{(1 + u - u_j^+ + 2u_0)^{(1-\alpha)}}{1 - \alpha} - \frac{(1 + 2u_0)^{(1-\alpha)}}{1 - \alpha} \right] + \bar{f}. \end{aligned} \quad (24) \quad \{\text{eq: e}\}$$

Similarly, because of the assumption (17a), Equation (10) becomes:

$$f_h(u, u_j^-) = k_b u + (k_a - k_b) \frac{(1 - u + u_j^- + 2u_0)^{(1-\alpha)}}{\alpha - 1}. \quad (25) \quad \{\text{eq: e}\}$$

Substituting the previous expression in Equation (8) and recalling (20), one obtains:

$$\begin{aligned} c^-(u, u_j^-) &= \beta_1 u^3 + \beta_2 u^5 + k_b u \\ &+ (k_a - k_b) \left[\frac{(1 - u + u_j^- + 2u_0)^{(1-\alpha)}}{\alpha - 1} - \frac{(1 + 2u_0)^{(1-\alpha)}}{\alpha - 1} \right] - \bar{f}. \end{aligned} \quad (26) \quad \{\text{eq: e}\}$$

Expression of \bar{f}

The expression of \bar{f} can be obtained by using Equation (11) or (12). Adopting (23), the former equation becomes:

$$\begin{aligned} k_b (u_j^+ - 2u_0) + \frac{(k_a - k_b)}{1 - \alpha} + 2k_b u_0 + 2\bar{f} - k_b u_j^+ \\ - (k_a - k_b) \frac{(1 + 2u_0)^{(1-\alpha)}}{1 - \alpha} = 0, \end{aligned} \quad (27) \quad \{\text{eq: e}\}$$

from which we obtain:

$$\bar{f} = \frac{k_a - k_b}{2} \left[\frac{(1 + 2u_0)^{(1-\alpha)} - 1}{1 - \alpha} \right]. \quad (28) \quad \{\text{eq: e}\}$$

Being $k_a > k_b$, $\alpha \neq 1$, and $u_0 > 0$, the previous expression provides a positive value of \bar{f} .

Table 1
Hysteresis loop shapes simulated by the AM

shape type	obtained for	
S1	$\beta_1 = \beta_2 = 0$	
S2	$\beta_1/\beta_2 > 0$	with $\beta_1 > 0$ and $\beta_2 > 0$
S3	$\beta_1/\beta_2 > 0$	with $\beta_1 < 0$ and $\beta_2 < 0$
S4	$\beta_1/\beta_2 < 0$	with $\beta_1 < \beta_2$
S5	$\beta_1/\beta_2 < 0$	with $\beta_1 > \beta_2$

Table 2
AM parameters

	k_a	k_b	α	β_1	β_2
(a)	100	10	20	0	0
(b)	100	10	20	2	2
(c)	100	10	20	-1.5	-1.5
(d)	100	10	20	-10	10

4.1.3. History variable

Invoking (20) and (23), Equation (13) specializes to:

$$\beta_1 u_P^3 + \beta_2 u_P^5 + k_b u_P + (k_a - k_b) \frac{(1 + u_P - u_j^+ + 2u_0)^{(1-\alpha)}}{1 - \alpha} + k_b u_j^+ + \bar{f} - k_b u_j^+ - (k_a - k_b) \frac{(1 + 2u_0)^{(1-\alpha)}}{1 - \alpha} = f_P, \quad (29)$$

from which the following expression of the history variable, holding for the loading case, is obtained:

$$u_j^+ = 1 + u_P + 2u_0 - \left\{ \frac{1 - \alpha}{k_a - k_b} [f_P - \beta_1 u_P^3 - \beta_2 u_P^5 - k_b u_P - \bar{f} + (k_a - k_b) \frac{(1 + 2u_0)^{(1-\alpha)}}{1 - \alpha}] \right\}^{\frac{1}{1-\alpha}}. \quad (30)$$

Similarly, using (20) and (25), Equation (14) becomes:

$$\beta_1 u_P^3 + \beta_2 u_P^5 + k_b u_P + (k_a - k_b) \frac{(1 - u_P + u_j^- + 2u_0)^{(1-\alpha)}}{\alpha - 1} + k_b u_j^- - \bar{f} - k_b u_j^- - (k_a - k_b) \frac{(1 + 2u_0)^{(1-\alpha)}}{\alpha - 1} = f_P, \quad (31)$$

from which the following expression of the history variable, valid for the unloading case, is obtained:

$$u_j^- = -1 + u_P - 2u_0 + \left\{ \frac{\alpha - 1}{k_a - k_b} [f_P - \beta_1 u_P^3 - \beta_2 u_P^5 - k_b u_P + \bar{f} + (k_a - k_b) \frac{(1 + 2u_0)^{(1-\alpha)}}{\alpha - 1}] \right\}^{\frac{1}{1-\alpha}}. \quad (32)$$

According to the coordinates of point P , that is, the initial

point of the generic loading (unloading) curve, the history variable u_j^+ (u_j^-) may assume positive or negative values.

4.2. Hysteresis Loop Shapes

As shown in Table 1, the proposed model is able to reproduce force-displacement hysteresis loops with five different shapes depending on the values assumed by the parameters β_1 and β_2 . Figure 9 presents four hysteresis loops having shape type S1, S2, S3, and S4, respectively, obtained by applying a sinusoidal transverse displacement of unit amplitude and simulated by adopting the Algebraic Model parameters listed in Table 2. The fifth type of shape, namely, S5, has not been presented since it is not of interest in this paper.

Specifically, Figure 9a shows a hysteresis loop bounded by two straight lines, whereas Figures 9b, 9c, and 9d show hysteresis loops bounded by two curves. The hysteresis loop of Figure 9a (9b) is typical of bolted SREBs deforming at relatively large (at large) shear strains, that is, $\gamma \leq 100-150\%$ ($\gamma > 100-150\%$), whereas the one of Figure 9c (9d) is typically displayed by unbonded FREBs when $\gamma \leq 100-150\%$ ($\gamma > 100-150\%$).

Figure 10 illustrates the sensitivity of each parameter of the proposed model in affecting the size and/or shape of hysteresis loops simulated by imposing a sinusoidal transverse displacement having unit amplitude and frequency. More specifically, the hysteresis loops in Figure 10a have been obtained setting $k_b = 10$, $\alpha = 20$, $\beta_1 = 0$, $\beta_2 = 0$, and using three values of k_a , that is, 50, 100, and 200. It is clear that the variation of k_a produces a variation of the hysteresis loop size without affecting its shape; in particular, the larger is k_a , the larger is the hysteresis loop size.

Figure 10b presents hysteresis loops simulated adopting $k_a = 100$, $\alpha = 20$, $\beta_1 = 0$, $\beta_2 = 0$, and three values of k_b , that is, 5, 10, and 15. It is evident that the variation of k_b produces a rotation of the hysteresis loop and a slight modification of its size. Specifically, if k_b is increased, the hysteresis loop rotates counter-clockwise and its size slightly decreases.

The hysteresis loops in Figure 10c have been simulated using $k_a = 100$, $k_b = 10$, $\beta_1 = 0$, $\beta_2 = 0$, and adopting three values of α , that is, 10, 20, and 40. It can be seen that the variation of α produces a variation of the hysteresis loop size without affecting its shape; in particular, the larger is α , the smaller is the hysteresis loop size.

Finally, Figures 10d, 10e, and 10f show how the parameter β_1 affects the shape of hysteresis loops having shape type S2, S3, and S4, respectively. The hysteresis loops in Figure 10d (10e) have been obtained adopting $k_a = 100$, $k_b = 10$, $\alpha = 20$, $\beta_2 = 2$ ($\beta_2 = -1.5$), and three values of β_1 , that is, 0.5, 2, and 4 (-0.5, -1.5, -4), whereas the hysteresis loops in Figure 10f have been obtained setting $k_a = 100$, $k_b = 10$, $\alpha = 20$, $\beta_2 = 10$, and adopting three values of β_1 , that is, -5, -10, and -15.

Since the influence of parameter β_2 on the shape of hysteresis loops characterized by a shape type S2, S3, or S4 is similar to the one displayed by β_1 , the related figures are omitted for brevity.

It has to be noted that an important benefit of the Algebraic Model consists in the accurate determination of its parameters through an analytical fitting of the experimental hysteresis

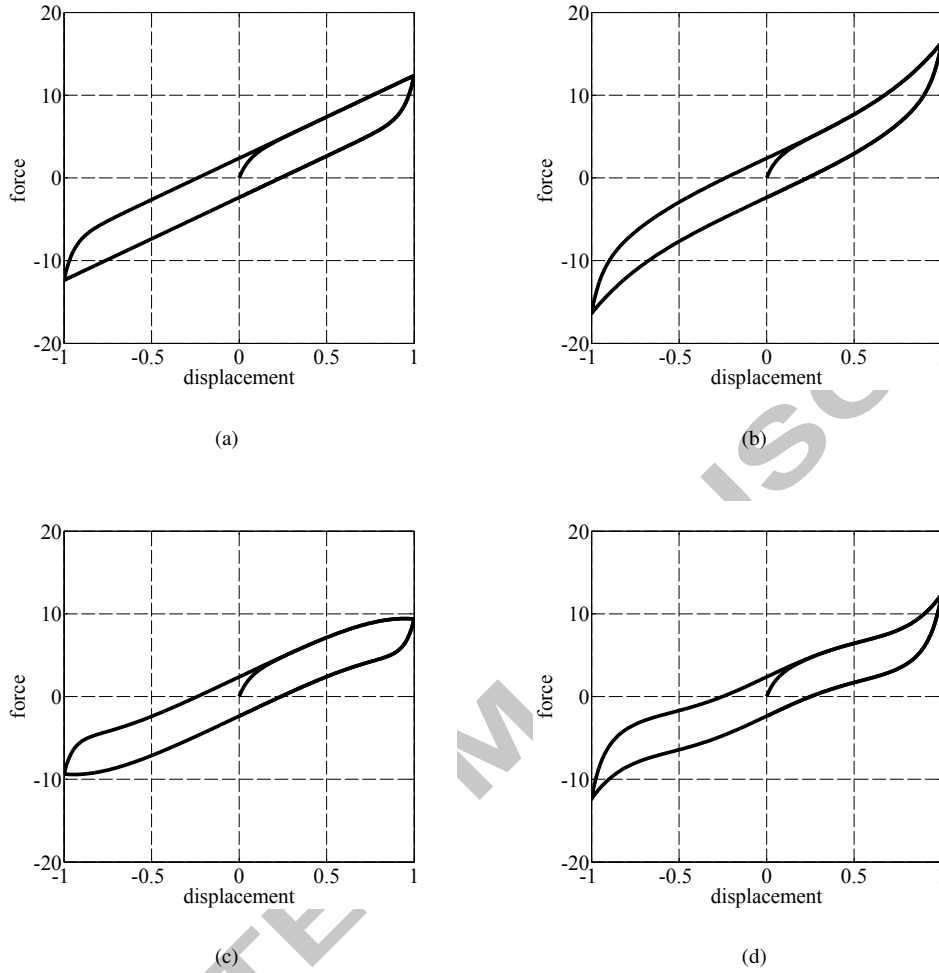


Figure 9: Hysteresis loops, having shape S1 (a), S2 (b), S3 (c), and S4 (d), defined in Table 1, simulated by adopting the AM parameters given in Table 2

loops. Indeed, as it has been shown in Figure 10, the Algebraic Model parameters are directly associated with the graphical properties of the hysteresis loop. If more accurate identifications are required, usually of nonlinear nature, such computed parameters represent suitable first trial values for the iterations required to compute the optimal parameters, that is, the ones that best fit the experimental data according to the adopted criterion. Moreover, the peculiar analytical formulation of the proposed model permits a closed form computation of the response gradient, an issue of the utmost importance in identification procedures.

4.3. Computer Implementation

To allow for an easy computer implementation, Table 3 presents a schematic flowchart of the Algebraic Model. To this end, we suppose that a seismic isolation device is subjected to a given transverse displacement history and that a displacement-driven solution scheme has been adopted. Because of these assumptions, the displacements $u_{t-\Delta t}$ and u_t , the velocities $\dot{u}_{t-\Delta t}$ and \dot{u}_t , as well as the restoring force $f_{t-\Delta t}$ are known over a time step Δt , and the restoring force f_t has to be evaluated.

The implementation scheme of the Algebraic Model, summarized in Table 3, is composed of two parts. In the first one, called *Initial settings*, the five model parameters, that is, k_a , k_b , α , β_1 , and β_2 , are assigned and the internal ones, namely, u_0 and \bar{f} , are evaluated. In the second one, called *Calculations at each time step*, the history variable u_j^+ (u_j^-) is updated if the sign of the transverse velocity at time t , that is, $s_t = \text{sgn}(\dot{u}_t)$, changes with respect to the one at $t - \Delta t$; then, the restoring force f_t is computed by using the expression of the generic loading (unloading) curve c^+ (c^-) if $u_j^+ - 2u_0 \leq u_t < u_j^+$ ($u_j^- < u_t \leq u_j^- + 2u_0$); otherwise, it is computed by adopting the expression of the upper (lower) limiting curve c_u (c_l).

5. Verification of the Proposed Model

This section presents the validation of the Algebraic Model, developed in Section 4. Specifically, the experimental verification is first carried out by comparing the results predicted analytically with some experimental results selected from the literature. Then, the numerical accuracy as well as the computational efficiency of the Algebraic Model are assessed by

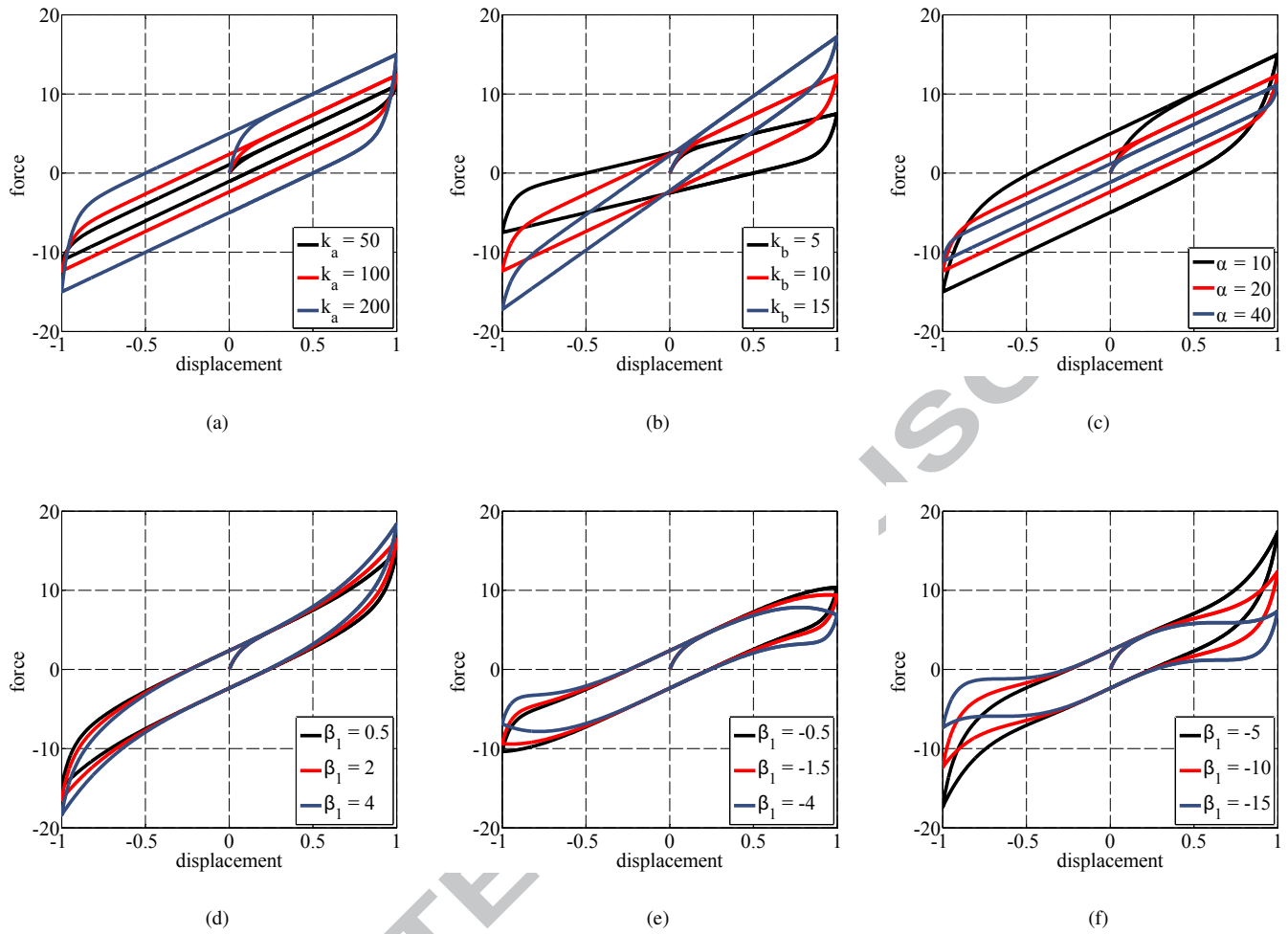


Figure 10: Influence of the AM parameters on the size and/or shape of the hysteresis loops

performing nonlinear time history analyses on a single degree of freedom mechanical system and comparing the results with those obtained by using a modified version of the celebrated Bouc-Wen model [16–18].

5.1. Experimental Verification

The hysteretic behavior of elastomeric bearings, deforming along one of their transverse directions under the effect of a constant axial compressive load, is strongly influenced by the shear strain attained by the bearing, generally defined as the ratio of the device transverse displacement to the total thickness of the rubber layers, as well as by the axial load.

In the sequel, the proposed Algebraic Model is employed for the simulation of the experimental hysteretic behavior characterizing several elastomeric bearings, that is, bolted SREBs and unbonded FREBs, that have been tested at various shear strain ranges under the effect of several axial compressive loads.

5.1.1. Simulation of the hysteretic behavior at various shear strain ranges

In order to demonstrate the capability of the Algebraic Model to predict the hysteretic behavior of elastomeric bearings subjected to a harmonic transverse motion having different amplitudes, under the effect of a constant axial compressive load, the results analytically predicted are compared to the experimental ones. In particular, the experimental hysteresis loops, adopted for the experimental verification of the model, are those obtained during the dynamic experimental tests conducted on a bolted SREB by Tsai et al. [20], and on an unbonded FREB by Kelly and Takhirov [4].

The SREB tested by Tsai et al. [20] is a HDRB having a square transverse cross section, with dimensions 106 mm × 106 mm, a total height of 65 mm, and a total thickness of rubber layers of 41 mm. Each experimental test, conducted on the bearing at the Chung-Shan Institute of Science and Technology, Taiwan, consisted in imposing five cycles of sinusoidal transverse displacement, having specified amplitude and frequency, under the effect of three different axial loads.

The FREB tested by Kelly and Takhirov [4] has a circu-

Table 3

AM Algorithm

1. Initial settings.	
1.1	Set the five model parameters: k_a , k_b , α , β_1 , and β_2 .
1.2	Compute the internal model parameters [see (19) and (28)]: $u_0 = \frac{1}{2} \left[\left(\frac{k_a - k_b}{\delta_k} \right)^{\frac{1}{\alpha}} - 1 \right]$ and $\bar{f} = \frac{k_a - k_b}{2} \left[\frac{(1+2u_0)^{(1-\alpha)} - 1}{1-\alpha} \right]$, with $\delta_k = 10^{-20}$.
2. Calculations at each time step.	
2.1	If $s_t s_{t-\Delta t} < 0$, update the history variable [see (30) and (32)]: $u_j = u_{t-\Delta t} + s_t (1 + 2u_0) - s_t \left\{ \frac{s_t(1-\alpha)}{k_a - k_b} \left[f_{t-\Delta t} - \beta_1 u_{t-\Delta t}^3 - \beta_2 u_{t-\Delta t}^5 - k_b u_{t-\Delta t} - s_t \bar{f} + (k_a - k_b) \frac{(1+2u_0)^{(1-\alpha)}}{s_t(1-\alpha)} \right] \right\}^{\left(\frac{1}{1-\alpha}\right)}$
2.2	Evaluate the restoring force at time t : if $u_j s_t - 2u_0 \leq u_t s_t < u_j s_t$: $f_t = \beta_1 u_t^3 + \beta_2 u_t^5 + k_b u_t + (k_a - k_b) \left[\frac{(1+s_t u_t - s_t u_j + 2u_0)^{(1-\alpha)}}{s_t(1-\alpha)} - \frac{(1+2u_0)^{(1-\alpha)}}{s_t(1-\alpha)} \right] + s_t \bar{f}$ [see (24) and (26)], otherwise: $f_t = \beta_1 u_t^3 + \beta_2 u_t^5 + k_b u_t + s_t \bar{f}$ [see (21) and (22)].

lar transverse cross section, with diameter of 305 mm, a total height of 140 mm, and a total thickness of rubber layers of 102 mm. Each experimental test, conducted on the device at the laboratory of the Pacific Earthquake Engineering Research Center of the University of California at Berkeley, consisted in imposing three cycles of sinusoidal transverse displacement, having specified amplitude and frequency, under the effect of two different axial loads.

Figure 11a (11b) shows the comparisons of the analytical and experimental results obtained by applying, to the above-described SREB (FREB), five (three) cycles of sinusoidal transverse displacement at three different amplitude levels, corresponding to a shear strain, γ , of 50%, 100%, and 150%, respectively, under the effect of an axial compressive load, f_v , of 29.42 kN (252.06 kN). In the case of the SREB, the frequency of the applied sinusoidal transverse displacement is constant and equal to 0.2 Hz for all the three amplitude levels, whereas, in the case of the FREB, it is equal to 0.5 Hz, 0.25 Hz, and 0.15 Hz for $\gamma = 50\%$, $\gamma = 100\%$, and $\gamma = 150\%$, respectively.

It can be observed that the agreement between the experimental hysteresis loops and the analytical ones, simulated by adopting the Algebraic Model parameters listed in Table 4, is satisfactory. In particular, it is proved that the proposed model is capable of well predicting the increase of the tangent stiffness that occurs in the tested SREB, due to strain crystallization of the rubber matrix, as well as in the tested FREB, due to the full rollover.

To better explain further features of the proposed model, the same experimental results are analytically predicted by means of a modified version of the celebrated Bouc-Wen model [16–18]. Among existing phenomenological models available in the literature, such a differential model, referred to as the Modified Bouc-Wen Model (MBWM), seems to be one of the most

suitable to perform nonlinear time history analyses of actual base-isolated structures, since it allows for an accurate prediction of the hysteretic response of elastomeric bearings by using a relatively small number of parameters that remain constant throughout the analysis.

In particular, according to this differential model, the restoring force of an elastomeric bearing is given by:

$$f(u) = a_1 u + a_2 |u| u + a_3 u^3 + a_4 |u| u^3 + a_5 u^5 + b \left(1 - \frac{\beta}{A} |z|^n \right) z, \quad (33) \quad \{\text{eq: e}$$

where z is a dimensionless variable obtained by solving the following first-order nonlinear ordinary differential equation:

$$\dot{z} = Y^{-1} (A\dot{u} - \beta\dot{u}|z|^n - \gamma|\dot{u}|z|z|^{n-1}), \quad (34) \quad \{\text{eq: e}$$

whereas, a_1 , a_2 , a_3 , a_4 , a_5 , b , Y , A , β , γ , and n represent the model parameters to be calibrated from experimental tests.

It is worth to notice that the above-described differential model represents the one specifically proposed by Chen and Ahmadi [19] (Manzoori and Toopchi-Nezhad [21]) for predicting the hysteretic behavior of HDRBs (FREBs), if the parameters a_4 and a_5 (a_2 and a_4) are set equal to zero.

Figure 12a (12b) compares the experimental hysteresis loops of the tested SREB (FREB) with those analytically predicted by employing the Modified Bouc-Wen Model and adopting the model parameters listed in Table 5.

The comparisons of Figures 11 and 12 as well as of Tables 4 and 5 hint at two important considerations. Firstly, the proposed Algebraic Model is as accurate as the Modified Bouc-Wen Model but offers the significant advantage of requiring a smaller number of parameters; indeed, as clearly shown by Tables 4 and 5, the proposed model needs the evaluation of only

Table 4
AM parameters adopted for simulating hysteresis loops in Figure 11

	k_a [Nm^{-1}]	k_b [Nm^{-1}]	α	β_1 [Nm^{-3}]	β_2 [Nm^{-5}]
(a)	41×10^4	78×10^3	130	10×10^6	20×10^8
(b)	12×10^5	36×10^4	50	-20×10^6	67×10^7

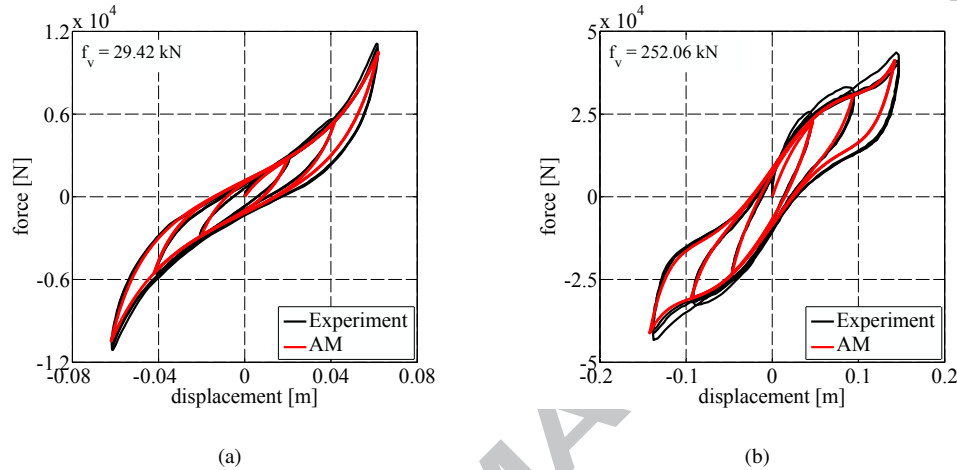


Figure 11: Comparisons of experimental and analytical hysteresis loops, simulated by using the AM parameters given in Table 4: SREB (a) and FREB (b)

five parameters, whereas the number of parameters to be identified in the Modified Bouc-Wen Model is equal to eleven.

Furthermore, both models are capable of simulating, with satisfactory approximation, the hysteresis loops at various shear strain ranges by adopting only one set of parameters, identified with respect to all the filtered experimental hysteresis loops. To be very meticulous, it has to be pointed out that the use of such a set of model parameters leads to the simulation of hysteresis loops that are slightly larger than the experimental ones, within the relatively large shear strain range, that is, $\gamma \leq 100\%$. This modeling aspect is typical of many other phenomenological models available in the literature, such as the Hwang et al. model, that has been proposed by Hwang et al. [13] for the simulation of the hysteretic behavior of SREBs and has been also adopted by Toopchi-Nezhad et al. [10] to predict the response of FREBs.

5.1.2. Simulation of the hysteretic behavior under several axial loads

In order to demonstrate the capability of the Algebraic Model to predict the hysteretic behavior of elastomeric bearings subjected to a harmonic transverse motion, under the effect of several constant axial compressive loads, the results analytically predicted are compared to the experimental ones. In particular, the experimental hysteresis loops, adopted for the experimental verification of the model, are those obtained during the dynamic experimental tests conducted on a bolted SREB by Tsai et al. [20], already described in 5.1.1, and on an unbonded FREB by De Raaf et al. [34].

The FREB tested by De Raaf et al. [34] has a square transverse cross section, with dimensions $70 \text{ mm} \times 70 \text{ mm}$, a total height of 24 mm , and a total thickness of rubber layers of 19 mm . Each experimental test consisted in imposing two cycles of sinusoidal transverse displacement, having specified amplitude and frequency, under the effect of four different axial loads.

Figure 13a (13b) shows the comparisons of the analytical and experimental results obtained by applying, to the above-described SREB (FREB), five (two) cycles of sinusoidal transverse displacement, having an amplitude corresponding to a shear strain, γ , of 150% , and a frequency equal to 0.3 Hz (0.67 Hz), under the effect of an axial compressive load, f_v , of 9.81 kN (7.84 kN). Figure 14a (14b) shows the same comparisons with the only difference that the axial compressive load, f_v , is equal to 29.42 kN (30 kN).

It can be observed that the agreement between the experimental hysteresis loops and the analytical ones, simulated in Figure 13 (14) by adopting the Algebraic Model parameters listed in Table 6 (7), is satisfactory. Thus, it is proved that the proposed model is capable of well predicting the complex hysteretic behavior displayed by the tested elastomeric bearings under the effect of several axial compressive loads.

5.2. Numerical Verification and Computational Efficiency

In this subsection, the nonlinear dynamic response of a single degree of freedom mechanical system, that is, a base-isolated rigid block, is simulated by modeling the restoring force of each seismic isolation device on the basis of the Algebraic Model.

Table 5

MBWM parameters adopted for simulating hysteresis loops in Figure 12

	A	n	b [N]	Y [m]	β	γ	a_1 [Nm ⁻¹]	a_2 [Nm ⁻²]	a_3 [Nm ⁻³]	a_4 [Nm ⁻⁴]	a_5 [Nm ⁻⁵]
(a)	1	1.1	1400	75×10^{-4}	0.1	0.9	78×10^3	-30×10^4	22×10^6	0	0
(b)	1	1.1	9350	21×10^{-3}	0.1	0.9	36×10^4	0	-20×10^6	0	67×10^7

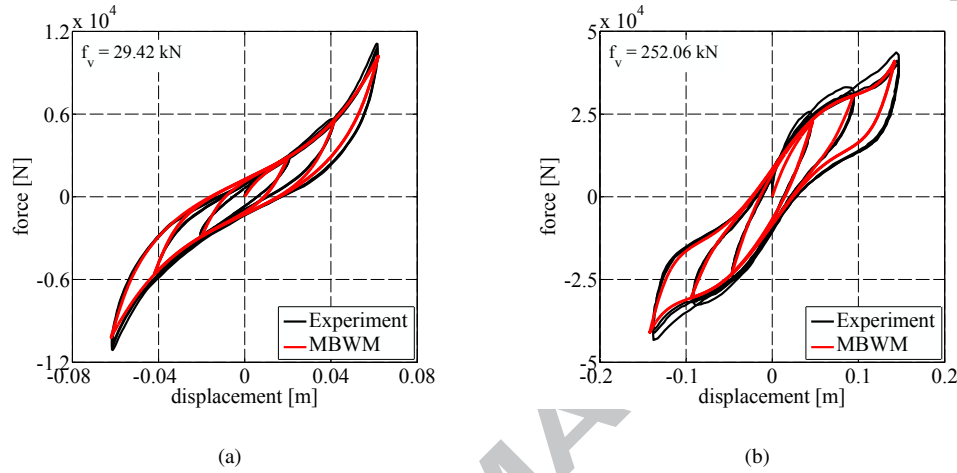


Figure 12: Comparisons of experimental and analytical hysteresis loops, simulated by using the MBWM parameters given in Table 5: SREB (a) and FREB (b)

In order to confirm the numerical accuracy of the proposed model and demonstrate its notable computational efficiency, the results of the nonlinear time history analyses and the corresponding computational times are compared with those obtained by modeling the restoring force of the seismic isolation bearings with the Modified Bouc-Wen Model described in 5.1.1. Such nonlinear time history analyses are performed for two different external forces, that is, a harmonic and an earthquake force.

5.2.1. Analyzed mechanical system

Figure 15 illustrates the analyzed mechanical system that consists of a rigid block isolated by two FREBs placed between a shaking table and the rigid block with no bonding at their upper and lower contact surfaces.

The motion of such a system, characterized by a single degree of freedom, is described by the equation:

$$m\ddot{u} + 2c\dot{u} + 2f(u) = p(t), \quad (35)$$

where m denotes the mass of the rigid block, c the viscous damping coefficient of each bearing, u , \dot{u} , and \ddot{u} the mechanical system displacement, velocity, and acceleration relative to the ground, respectively, f the restoring force of each unbonded FREB, and p the external force depending upon time t .

If the mechanical system is subjected to an earthquake excitation, p represents the effective earthquake force, that is, a force acting opposite to the acceleration and equal to mass m times the ground acceleration \ddot{u}_g . Thus, the nonlinear ordinary

differential equation (35) is replaced by:

$$m\ddot{u} + 2c\dot{u} + 2f(u) = -m\ddot{u}_g(t). \quad (36)$$

The rigid block has a mass of $51388.36 \text{ N s}^2 \text{ m}^{-1}$, whereas the two unbonded FREBs, characterized by negligible mass and viscous damping coefficient, have the same properties as the one tested by Kelly and Takhirov [4] and described in 5.1.1. Therefore, their nonlinear behavior is simulated by adopting the Algebraic Model (Modified Bouc-Wen Model) parameters listed in Table 4 (Table 5).

5.2.2. Applied external forces

The nonlinear dynamic response of the mechanical system is evaluated for two different external forces, namely, a harmonic force and an earthquake force.

The harmonic force, shown in Figure 16a, is a sinusoidal force characterized by an amplitude p_0 that increases linearly with time from 0 to 10^5 N , a forcing frequency $\omega_p = 2\pi \text{ rad/s}$, and a time duration $t_d = 10 \text{ s}$.

The earthquake force, shown in Figure 16b, is evaluated by adopting the SN component of horizontal ground acceleration recorded at the Jensen Filter Plant station during the Northridge earthquake of January 17, 1994. The original ground acceleration record, having time step equal to 0.005 s , has been scaled by a factor of $1/2$ in order to reach a peak mechanical system displacement, relative to the ground, that is close to the maximum displacement attained by the unbonded FREB during the experimental tests conducted by Kelly and Takhirov [4].

Table 6

AM parameters adopted for simulating hysteresis loops in Figure 13

	k_a [Nm^{-1}]	k_b [Nm^{-1}]	α	β_1 [Nm^{-3}]	β_2 [Nm^{-5}]
(a)	68×10^4	98×10^3	250	60×10^5	16×10^8
(b)	34×10^4	79×10^3	400	-68×10^6	45×10^9

Table 7

AM parameters adopted for simulating hysteresis loops in Figure 14

	k_a [Nm^{-1}]	k_b [Nm^{-1}]	α	β_1 [Nm^{-3}]	β_2 [Nm^{-5}]
(a)	68×10^4	80×10^3	220	94×10^5	22×10^8
(b)	40×10^4	55×10^3	400	-38×10^6	30×10^9

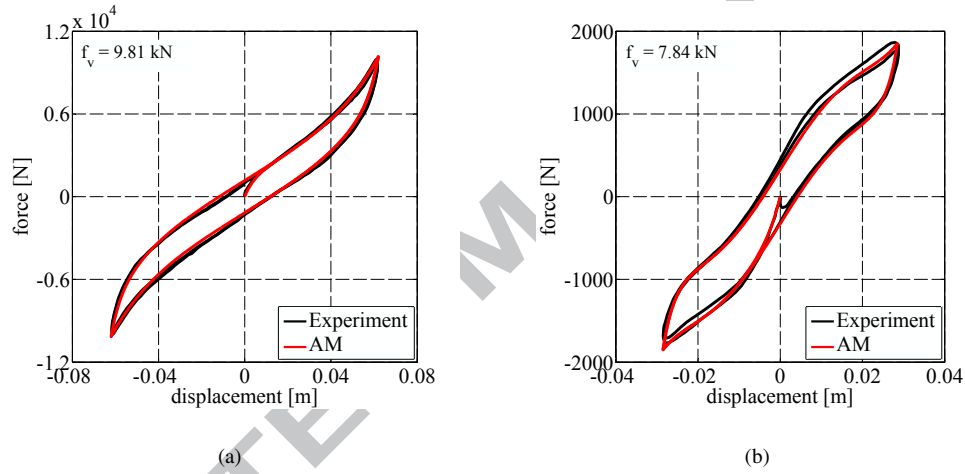


Figure 13: Comparisons of experimental and analytical hysteresis loops, simulated by using the AM parameters given in Table 6: SREB (a) and FREB (b)

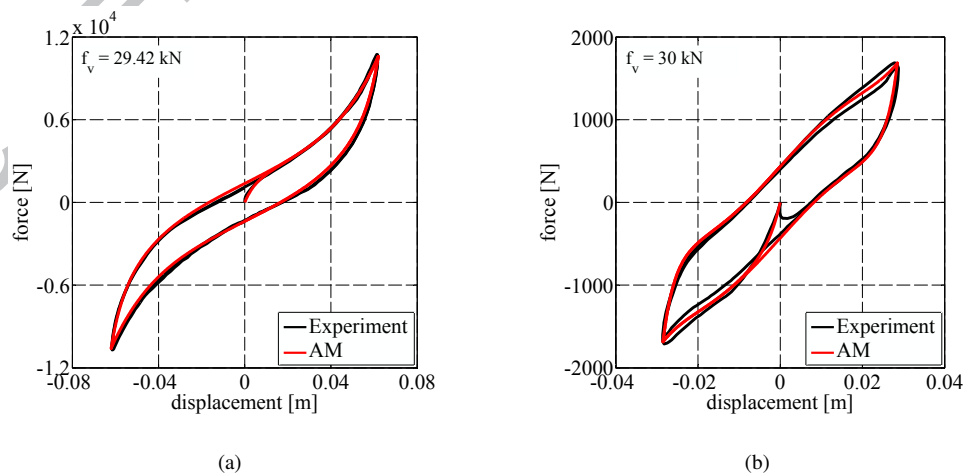


Figure 14: Comparisons of experimental and analytical hysteresis loops, simulated by using the AM parameters given in Table 7: SREB (a) and FREB (b)

5.2.3. Results of the nonlinear time history analyses

In the sequel, the results of some numerical simulations are presented to assess the numerical accuracy and the computa-

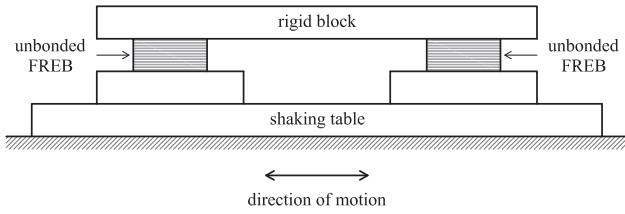
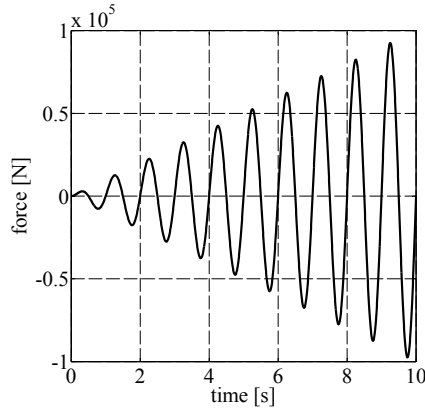
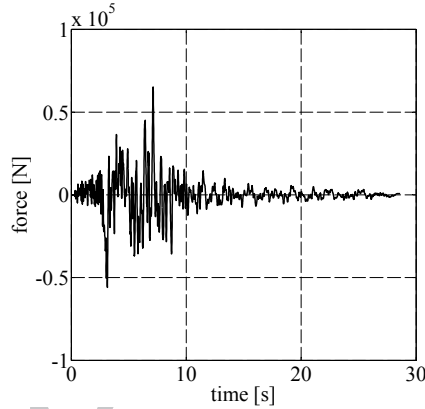


Figure 15: Mechanical system adopted for the numerical verification



(a)



(b)

Figure 16: Applied external forces: harmonic (a) and earthquake force (b)

tional efficiency of the Algebraic Model.

The equation of motion, given by Equation (35) or (36), according to the type of applied external force, has been numerically solved by employing a widely used explicit time integration method, that is, the central difference method [41, 42], and adopting a time step of 0.005 s. In addition, the first-order nonlinear ordinary differential equation characterizing the Modified Bouc-Wen Model, given by Equation (34), has been numerically solved by adopting the unconditionally stable semi-implicit Runge-Kutta method [23] and using 50 steps. The

numerical time integration algorithm as well as the hysteretic models have been implemented in MATLAB and run on a computer having an Intel®Core™i7-4700MQ processor and a CPU at 2.40 GHz with 16 GB of RAM.

Tables 8 and 9 present the results of the Nonlinear Time History Analyses (NLTHAs) obtained for the harmonic and earthquake forces, respectively.

The numerical results confirm the accuracy of the Algebraic Model since the maximum and minimum values of the relative displacement, velocity, and acceleration of the mechanical system, evaluated by employing the proposed model, are quite close to those predicted by the Modified Bouc-Wen Model.

Furthermore, the numerical results also show that the computational burden of the Algebraic Model, expressed by the total computational time t_{ct} , is significantly smaller than the one characterizing the Modified Bouc-Wen Model. Since the parameter t_{ct} depends upon the amount of the back-ground process running on the computer, the relevant memory, as well as the CPU speed, a fully objective measure of the computational benefits, associated with the use of the Algebraic Model with respect to the Modified Bouc-Wen Model, is obtained by normalizing such a parameter as follows:

$$AM_{tctp} [\%] = \frac{AM_{tct}}{MBWM_{tct}} \cdot 100. \quad (37) \quad \{\text{eq: e}$$

Figures 17, 18, and 19 illustrate, respectively, the time histories of the relative displacement, velocity, and acceleration of the mechanical system, whereas Figure 20 shows the restoring force-displacement hysteresis loops displayed by each FREQ. Generally speaking, the comparison between the responses simulated with the Algebraic Model and the Modified Bouc-Wen Model shows a very good agreement.

6. Conclusions

We have presented a uniaxial phenomenological model, able to simulate the complex hysteretic behavior typically displayed by bolted SREBs and unbonded FREQs, deforming along one of their transverse directions under the effect of a constant moderate axial compressive load.

The proposed model, representing a specific instance of the class of uniaxial phenomenological models formulated by Viana et al. [24], requires only one history variable, is based on a set of only five parameters, directly associated with the graphical properties of the hysteresis loop, as shown by the sensitivity analysis carried out in 4.2, and can be easily implemented in a computer program, as shown by the schematic flowchart illustrated in 4.3.

For simplicity, in the paper, the model has been denominated Algebraic Model since the isolator restoring force, that is, the output variable of the model, is computed by solving an algebraic equation.

The proposed model has been validated by means of experimental tests and numerical simulations. Specifically, the experimental verification, performed by comparing the results

Table 8
NLTHAs results | Harmonic force

	tct [s]	$tctp$	u [m]		\dot{u} [ms ⁻¹]		\ddot{u} [ms ⁻²]	
			max	min	max	min	max	min
MBWM	9.463	-	0.1305	-0.1220	0.7967	-0.8409	4.9104	-5.1878
AM	0.066	0.69%	0.1302	-0.1221	0.7963	-0.8396	4.9151	-5.1878

Table 9
NLTHAs results | Earthquake force

	tct [s]	$tctp$	u [m]		\dot{u} [ms ⁻¹]		\ddot{u} [ms ⁻²]	
			max	min	max	min	max	min
MBWM	27.95	-	0.1421	-0.1124	0.4048	-0.3613	2.2892	-2.1137
AM	0.203	0.73%	0.1411	-0.1126	0.4037	-0.3594	2.2805	-2.1152

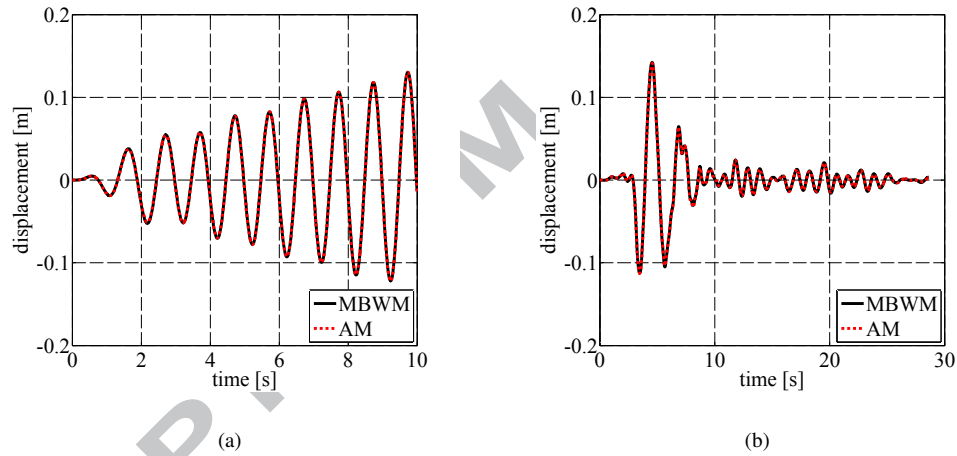


Figure 17: Relative displacement time history obtained by applying the harmonic (a) and earthquake force (b)

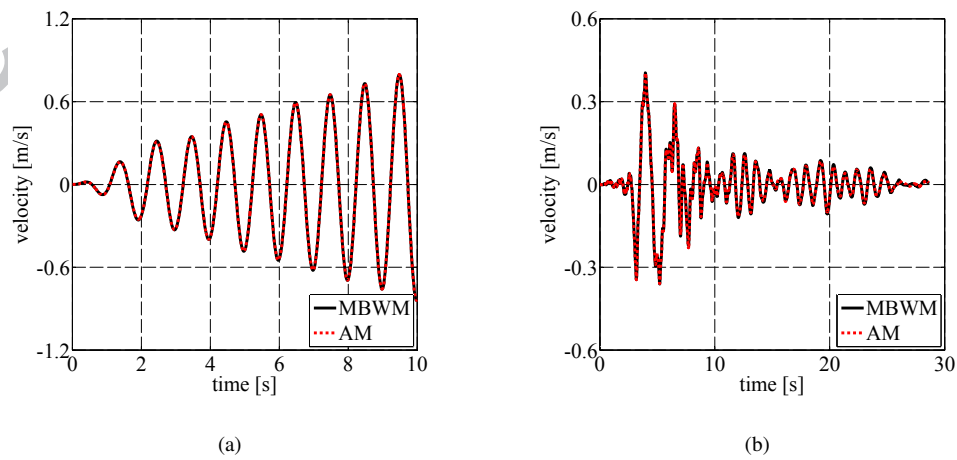


Figure 18: Relative velocity time history obtained by applying the harmonic (a) and earthquake force (b)

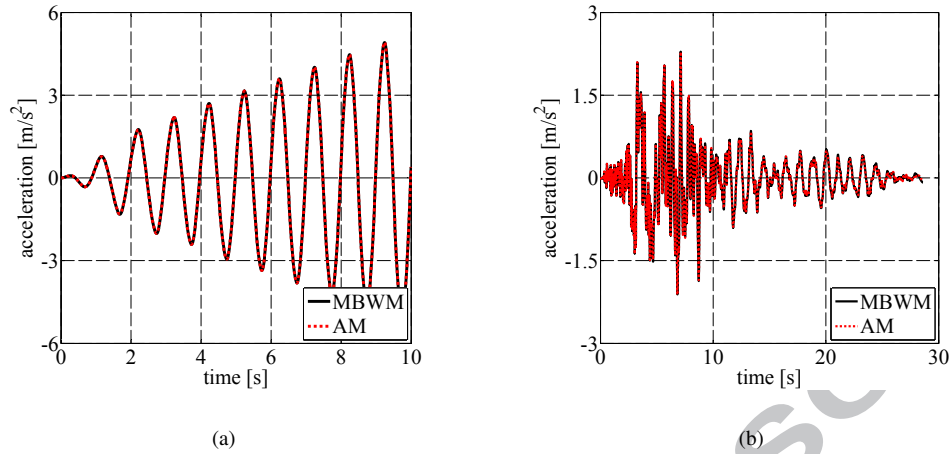


Figure 19: Relative acceleration time history obtained by applying the harmonic (a) and earthquake force (b)

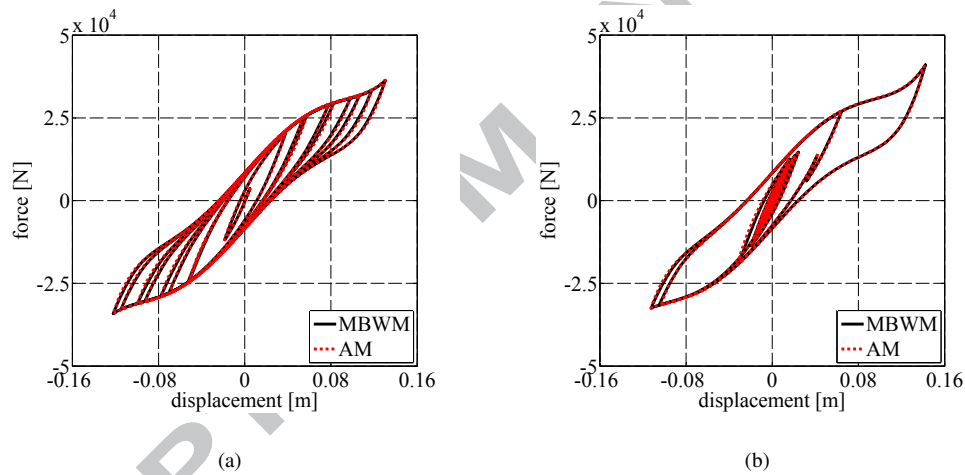


Figure 20: Restoring force-displacement hysteresis loops obtained by applying the harmonic (a) and earthquake force (b)

predicted analytically with some experimental results selected from the literature, reveals that:

- the model is able to simulate the hysteretic behavior displayed by the tested elastomeric bearings at various shear strain ranges; in particular, it well predicts the increase of the tangent stiffness occurring in the tested SREB (FREB) due to strain crystallization of the rubber matrix (rollover);
- the model is able to reproduce the complex hysteretic behavior displayed by the tested elastomeric bearings under the effect of several axial compressive loads.

The numerical accuracy and the computational efficiency of the proposed model have been assessed by performing nonlinear time history analyses on a single degree of freedom mechanical system, for two different external forces, that is, a harmonic force and an earthquake force, and comparing the results of the Algebraic Model with those associated with the Modified

Bouc-Wen Model. Specifically, the following conclusions can be drawn:

- the numerical results of the Algebraic Model closely match those predicted by the Modified Bouc-Wen Model, for both types of external force;
- the total computational time required by the Algebraic Model is equal to 0.69% (0.73%), for the harmonic (earthquake) force case, of the one associated with the Modified Bouc-Wen Model;
- the Modified Bouc-Wen Model needs the calibration of 11 parameters, whereas the Algebraic Model requires only 5 model parameters having a clear mechanical significance.

Current research is focusing on the extension of the proposed model to the two-dimensional case through the definition of an interaction domain involving restoring forces. In particular, by

assuming an isotropic transverse behavior of elastomeric bearings, a circular interaction function can be postulated to couple the restoring force-displacement responses along two orthogonal transverse directions under the effect of a constant moderate axial compressive load. Furthermore, in forthcoming papers, the presented model will be combined with recent strategies to address the nonlinear behavior of framed [43, 44] or shear wall structures [45, 46] in order to analyze base-isolated buildings by exploiting the concept of seismic response envelopes [47, 48].

Acknowledgments

The present research was supported by the Italian Government, ReLuis 2017 project [AQ DPC/ReLUIS 2014-2018, PR2, Task 2.3] and PRIN 2015 grants [2015JW9NJT-PE8, WP2 Task 2.1], which is gratefully acknowledged by the authors.

Data Availability

The raw and processed data required to reproduce these findings cannot be shared at this time due to technical limitations.

References

- [1] F. Naeim, J. Kelly, *Design of Seismic Isolated Structures: From Theory to Practice*, John Wiley and Sons Inc, Hoboken, NJ, USA, 1999.
- [2] M. Constantinou, A. Whittaker, Y. Kalpakidis, D. Fenz, G. Warn, Performance of seismic isolation hardware under service and seismic loading, Technical Report MCEER-07-0012, State University of New York, Buffalo, NY, USA.
- [3] H. Toopchi-Nezhad, M. Tait, R. Drysdale, Shake table study on an ordinary low-rise building seismically isolated with SU-FREIs (stable unbonded-fiber reinforced elastomeric isolators), *Earthquake Engineering and Structural Dynamics* 38 (11) (2009) 1335–1357.
- [4] J. Kelly, S. Takhirov, Analytical and experimental study of fiber-reinforced elastomeric isolators, PEER Report 2001/11, Pacific Earthquake Engineering Research Center, University of California, Berkeley, CA, USA.
- [5] H. Toopchi-Nezhad, M. Tait, R. Drysdale, Bonded versus unbonded strip fiber reinforced elastomeric isolators: finite element analysis, *Composite Structures* 93 (2) (2011) 850–859.
- [6] A. Das, A. Dutta, S. Deb, Modeling of fiber-reinforced elastomeric base isolators, in: *Proceedings of the 15th World Conference on Earthquake Engineering*, Lisbon, Portugal, 2012.
- [7] A. Das, A. Dutta, S. Deb, Performance of fiber-reinforced elastomeric base isolators under cyclic excitation, *Structural Control and Health Monitoring* 22 (2) (2015) 197–220.
- [8] M. Pauletta, A. Cortesia, I. Pitacco, G. Russo, A new bi-linear constitutive shear relationship for Unbonded Fiber-Reinforced Elastomeric Isolators (U-FREIs), *Composite Structures* 168 (2017) 725–738.
- [9] W.-H. Huang, G. Fenves, A. Whittaker, S. Mahin, Characterization of seismic isolation bearings for bridges from bi-directional testing, in: *Proceedings of the 12th World Conference on Earthquake Engineering*, New Zealand, 2000.
- [10] H. Toopchi-Nezhad, M. Tait, R. Drysdale, Simplified analysis of a low-rise building seismically isolated with stable unbonded fiber reinforced elastomeric isolators, *Canadian Journal of Civil Engineering* 36 (7) (2009) 1182–1194.
- [11] A. Markou, G. Manolis, Mechanical formulations for bilinear and trilinear hysteretic models used in base isolators, *Bulletin of Earthquake Engineering* 14 (12) (2016) 3591–3611.
- [12] M. Kikuchi, I. Aiken, An analytical hysteresis model for elastomeric seismic isolation bearings, *Earthquake Engineering and Structural Dynamics* 26 (2) (1997) 215–231.
- [13] J. Hwang, J. Wu, T.-C. Pan, G. Yang, A mathematical hysteretic model for elastomeric isolation bearings, *Earthquake Engineering and Structural Dynamics* 31 (4) (2002) 771–789.
- [14] G. Serino, A parallel elasto-plastic model for nonlinear bidirectional analysis of base asymmetric isolated structures, in: *Proceedings of the European Workshop on the Seismic Behaviour of Asymmetric and Setback Structures*, Capri, Italy, 1996.
- [15] S. Nagarajaiah, A. Reinhorn, M. Constantinou, Nonlinear dynamic analysis of 3-D base-isolated structures, *Journal of Structural Engineering*, ASCE 117 (7) (1991) 2035–2054.
- [16] R. Bouc, Modele mathematique d'hysteresis, *Acustica* 24 (1971) 16–25.
- [17] Y. Wen, Method for random vibration of hysteretic systems, *Journal of the Engineering Mechanics Division*, ASCE 102 (2) (1976) 249–263.
- [18] Y. Wen, Equivalent linearization for hysteretic systems under random excitation, *Journal of Applied Mechanics*, ASME 47 (1) (1980) 150–154.
- [19] Y. Chen, G. Ahmadi, Wind effects on base-isolated structures, *Journal of Engineering Mechanics*, ASCE 118 (8) (1992) 1708–1727.
- [20] C. Tsai, T. Chiang, B. Chen, S. Lin, An advanced analytical model for high damping rubber bearings, *Earthquake Engineering and Structural Dynamics* 32 (9) (2003) 1373–1387.
- [21] A. Manzoori, H. Toopchi-Nezhad, Application of an extended Bouc-Wen model in seismic response prediction of unbonded fiber-reinforced isolators, *Journal of Earthquake Engineering* 21 (1) (2017) 87–104.
- [22] A. Quarteroni, R. Sacco, F. Saleri, *Numerical Mathematics*, Springer-Verlag, New York, NY, USA, 2000.
- [23] H. Rosenbrock, Some general implicit processes for the numerical solution of differential equations, *The Computer Journal* 4 (1963) 329–330.
- [24] N. Vaiana, S. Sessa, F. Marmo, L. Rosati, A class of uniaxial phenomenological models for simulating hysteretic phenomena in rate-independent mechanical systems and materials, *Nonlinear Dynamics* 93 (3) (2018) 1647–1669.
- [25] M. Abe, J. Yoshida, Y. Fujino, Multiaxial behaviors of laminated rubber bearings and their modeling. I: Experimental study, *Journal of Structural Engineering*, ASCE 130 (8) (2004) 1119–1132.
- [26] Y. Al-Anany, M. Tait, Fiber reinforced elastomeric isolators for the seismic isolation of bridges, *Composite Structures* 160 (2017) 300–311.
- [27] I. Aiken, J. Kelly, P. Clark, K. Tamura, M. Kikuchi, T. Itoh, Experimental studies of the mechanical characteristics of three types of seismic isolation bearings, in: *Proceedings of the 10th World Conference on Earthquake Engineering*, Madrid, Spain, Vol. 4, 1992, pp. 2281–2286.
- [28] A. Mori, P. Moss, N. Cooke, A. Carr, The behavior of bearings used for seismic isolation under shear and axial load, *Earthquake Spectra* 15 (2) (1999) 199–224.
- [29] R. Skinner, W. Robinson, G. McVerry, *An Introduction to Seismic Isolation*, John Wiley and Sons Inc, Chichester, West Sussex, England, UK, 1993.
- [30] J. Kelly, Analysis of fiber-reinforced elastomeric isolators, *Journal of Seismology and Earthquake Engineering* 2 (1) (1999) 19–34.
- [31] H. Toopchi-Nezhad, M. Tait, R. Drysdale, Testing and modeling of square carbon fiber-reinforced elastomeric seismic isolators, *Structural Control and Health Monitoring* 15 (6) (2008) 876–900.
- [32] G. Russo, M. Pauletta, A. Cortesia, A study on experimental shear behavior of fiber-reinforced elastomeric isolators with various fiber layouts, elastomers and aging conditions, *Engineering Structures* 52 (2013) 422–433.
- [33] B.-Y. Moon, G.-J. Kang, B.-S. Kang, J. Kelly, Design and manufacturing of fiber reinforced elastomeric isolator for seismic isolation, *Journal of Materials Processing Technology* 130 (2002) 145–150.
- [34] M. de Raaf, M. Tait, H. Toopchi-Nezhad, Stability of fiber-reinforced elastomeric bearings in an unbonded application, *Journal of Composite Materials* 45 (18) (2011) 1873–1884.
- [35] H. Toopchi-Nezhad, M. Tait, R. Drysdale, Lateral response evaluation of fiber-reinforced neoprene seismic isolators utilized in an unbonded application, *Journal of Structural Engineering*, ASCE 134 (10) (2008) 1627–1637.
- [36] Y. Al-Anany, Fiber reinforced elastomeric isolators for bridge applications, Ph.D. Thesis, McMaster University, Hamilton, ON, Canada.
- [37] T.-C. Pan, G. Yang, Nonlinear analysis of base-isolated MDOF structures, in: *Proceedings of the 11th World Conference on Earthquake Engineering*, Mexico, 1996.
- [38] M. Abe, J. Yoshida, Y. Fujino, Multiaxial behaviors of laminated rubber

- bearings and their modeling. II: Modeling, *Journal of Structural Engineering*, ASCE 130 (8) (2004) 1133–1144.
- [39] N. Vaiana, Mathematical models and numerical methods for the simulation of the earthquake response of seismically base-isolated structures, Ph.D. Thesis, University of Naples Federico II, Naples, Italy.
- [40] N. Vaiana, M. Spizzuoco, G. Serino, Wire rope isolators for seismically base-isolated lightweight structures: experimental characterization and mathematical modeling, *Engineering Structures* 140 (2017) 498–514.
- [41] K. Bathe, *Finite Element Procedures*, Prentice Hall, Englewood Cliffs, NJ, USA, 1996.
- [42] F. Greco, R. Luciano, G. Serino, N. Vaiana, A mixed explicit-implicit time integration approach for nonlinear analysis of base-isolated structures, *Annals of Solid and Structural Mechanics* (2017). <https://doi.org/10.1007/s12356-017-0051-z>.
- [43] F. Marmo, L. Rosati, Analytical integration of elasto-plastic uniaxial constitutive laws over arbitrary sections, *International Journal for Numerical Methods in Engineering* 91 (9) (2012) 990–1022.
- [44] F. Marmo, L. Rosati, The fiber-free approach in the evaluation of the tangent stiffness matrix for elastoplastic uniaxial constitutive laws, *International Journal for Numerical Methods in Engineering* 94 (9) (2013) 868–894.
- [45] N. Valoroso, F. Marmo, S. Sessa, Limit state analysis of reinforced shear walls, *Engineering Structures* 61 (2014) 127–139.
- [46] N. Valoroso, F. Marmo, S. Sessa, A novel shell element for nonlinear pushover analysis of reinforced concrete shear walls, *Bulletin of Earthquake Engineering* 13 (8) (2015) 2367–2388.
- [47] S. Sessa, F. Marmo, L. Rosati, Effective use of seismic response envelopes for reinforced concrete structures, *Earthquake Engineering and Structural Dynamics* 44 (14) (2015) 2401–2423.
- [48] S. Sessa, F. Marmo, N. Vaiana, L. Rosati, A computational strategy for Eurocode 8 - compliant analyses of reinforced concrete structures by seismic envelopes, *Journal of Earthquake Engineering* (2018). <https://doi.org/10.1080/13632469.2018.1551161>.